Interannual and seasonal variability of biomass burning emissions constrained by satellite observations

Bryan N. Duncan,[1] Randall V. Martin,[2] Amanda C. Staudt,[3] Rosemarie Yevich, and Jennifer A. Logan

Department of Earth and Planetary Sciences and Division of Engineering and Applied Sciences, Harvard University, Cambridge, Massachusetts, USA

[1]   We present a methodology for estimating the seasonal and interannual variation of biomass burning designed for use in global chemical transport models. The average seasonal variation is estimated from 4 years of fire-count data from the Along Track Scanning Radiometer (ATSR) and 1–2 years of similar data from the Advanced Very High Resolution Radiometer (AVHRR) World Fire Atlases. We use the Total Ozone Mapping Spectrometer (TOMS) Aerosol Index (AI) data product as a surrogate to estimate interannual variability in biomass burning for six regions: Southeast Asia, Indonesia and Malaysia, Brazil, Central America and Mexico, Canada and Alaska, and Asiatic Russia. The AI data set is available from 1979 to the present with an interruption in satellite observations from mid-1993 to mid-1996; this data gap is filled where possible with estimates of area burned from the literature for different regions. Between August 1996 and July 2000, the ATSR fire-counts are used to provide specific locations of emissions and a record of interannual variability throughout the world. We use our methodology to estimate mean seasonal and interannual variations for emissions of carbon monoxide from biomass burning, and we find that no trend is apparent in these emissions over the last two decades, but that there is significant interannual variability.   *INDEX TERM:* 0365 Atmospheric Composition and Structure: Troposphere—composition and chemistry; *KEYWORDS:* Biomass burning, interannual seasonal variation

1. Introduction

[2] Biomass burning is a major source of many trace gases on a regional and a global scale [*Seiler and Crutzen*, 1980; *Logan et al.*, 1981; *Crutzen and Andreae*, 1990; *Andreae*, 1991]. Interannual variations in biomass burning within specific regions of the world can be dramatic, depending on factors such as rainfall and political incentives to clear land. The forest fires in Indonesia during 1997–1998 and those in Mexico during 1998, both related to the El Niño Southern Oscillation (ENSO) induced drought, are well known examples of extreme fire events [e.g., *Levine*, 1999; *Nakajima et al.*, 1999; *Peppler et al.*, 2000; *Cheng and Lin*, 2001]. While most burning occurs in the tropics, major fires can also occur in the Northern Hemisphere mid and high latitudes (e.g., the Great China Fire of 1987 [*Cahoon et al.*, 1991, 1994]). Information is available on the areas of fires in developed countries, but such data are sparse for the developing world. Published estimates of biomass burning emissions [*Crutzen and Andreae*, 1990; *Hao and Liu*, 1994; *Lobert et al.*, 1999; *Galanter et al.*, 2000] are generally for mean conditions. Estimates of the seasonality of biomass burning in the tropics have relied primarily on surrogates, such as seasonal rainfall patterns, cultural practices, vegetation types, and surface ozone [*Hao and Liu*, 1994; *Richardson*, 1994]. In the last twenty years, however, data have become available for smoke and fires detected by remote sensing [*Malingreau*, 1990; *Stricker et al.*, 1995; *Hsu et al.*, 1996; *Cooke et al.*, 1996; *Justice et al.*, 1996; *Herman et al.*, 1997; *Olson et al.*, 1999]. *Cooke et al.* [1996], for example, used fire-counts derived from Advanced Very High Resolution Radiometer (AVHRR) data for 1984 to 1989 to estimate the seasonal variation of biomass burning in Africa, while *Herman et al.* [1997] showed time series of biomass burning aerosols inferred from Total Ozone Mapping Spectrometer (TOMS) data for the same period for selected regions in South America and Africa. *Barbosa et al.* [1999] estimated the interannual variation of biomass burning emissions from Africa for 1985–1991 using AVHRR fire-counts, while *Dwyer et al.* [2000] conducted a global analysis of the temporal and spatial distribution of vegetation fires using AVHRR fire-counts from April 1992 to December 1993.

---

[1]Now at Laboratoire de Modélisation de la Chimie Atmosphérique, École Polytechnique Fédérale de Lausanne, Lausanne, Switzerland.

[2]Now at Harvard-Smithsonian Center for Astrophysics, Cambridge, Massachusetts, USA.

[3]Now at National Research Council, Washington, D. C., USA.

[3] In this paper we use remotely sensed data for fire-counts and for smoke-related aerosols to estimate both the seasonal variation and the interannual variation of biomass burning. The methodologies developed in this study are used to add time-dependency to biomass burning inventories in global 3-d chemical transport models. We employ two surrogates for the time dependence of biomass burning: (1) fire-counts [*Arino and Melinotte*, 1995; *Arino and Rosaz*, 1999] and (2) the TOMS Aerosol Index (AI) data product [*Hsu et al.*, 1996; *Herman et al.*, 1997; *Torres et al.*, 1998], a measure of the absorbing aerosol column derived by satellite observations. We evaluate the time dependence that we derive from the TOMS AI data with both fire-count data and with estimates of total area burned reported in the literature. We then apply the time dependence of biomass burning to an annual mean emissions inventory. The resulting time-dependent emissions inventory has been used in 3-d model studies of the emissions of aerosols from biomass burning [*Chin et al.*, 2002], pollution transport from Asia [*Staudt et al.*, 2001], ozone over Oceania [*Chandra et al.*, 2002], ozone in the tropics [*Martin et al.*, 2002a], and a retrieval of NO_2 from GOME [*Martin et al.*, 2002b]. It is currently being used in a study of the interannual variability of carbon monoxide (CO) [*Duncan et al.*, in preparation; *Duncan and Logan*, in preparation].

[4] We describe the satellite data sets in section 2 and identify some of their shortcomings for our objectives. Our method for estimating the mean seasonal variation of biomass burning from fire-counts from the Along Track Scanning Radiometer (ATSR) World Fire Atlas [*Arino and Rosaz*, 1999] and from AVHRR [*Arino and Melinotte*, 1995] is given in section 3.1. Our method for using TOMS AI data to estimate the long-term interannual variation of biomass burning follows in section 3.2. The fire-count data are used to prescribe the interannual variation of biomass burning in regions where the TOMS AI is not applicable, and to enhance the AI product for 1996 to 2000, as described in section 3.3. In section 4.1, we discuss important features of the mean seasonal variation of biomass burning by region, while we discuss the interannual variation of burning by region in section 4.2. Trends in and the regional contributions to global biomass burning emissions are discussed in section 5, and a summary is given in section 6.

2. Sources of Data

2.1. Fire-Count Data—AVHRR and ATSR

[5] Fire-counts provide a useful proxy for the seasonal variation of biomass burning [*Eva and Lambin*, 1998]. We use fire-count data from two satellite instruments, ATSR [*Arino and Rosaz*, 1999] and AVHRR [*Arino and Melinotte*, 1995]. The ATSR World Fire Atlas is available from the European Space Agency (ESA) for August 1996 through December 2000 as derived from ATSR-2 [*Stricker et al.*, 1995] on board the European Remote Sensing-2 satellite. The satellite was launched in 1995 into a Sun-synchronous orbit. The ATSR-2 instrument has an observation swath of 512 km, yielding a 3-day return time at the equator. Fire-counts are determined from nighttime (~10 pm local time) ATSR data observed in the 3.7 μm thermal channel and processed into a Gridded Brightness Temperature (GBT) product. Fire-counts are reported as the number of times the 3.7 μm channel exceeds

308 K. They have been shown to be correlated with the Polder Aerosol Index for biomass burning over land [*Goloub and Arino*, 2000] and have been more extensively validated under the coordination of the International Global-Biosphere Programme Data and Information System (IGBP-DIS) [*Arino and Plummer*, 2001, available at http://shark1.esrin.esa.it/ FIRE/AF/ATSR/]. They found that the geo-location and spatial extent of the hot spots are accurate, and there are few cases of warm surface detection that do not represent fires, e.g., hot deserts and cities. Gas flares are also detected.

[6] The AVHRR Fire Atlas is available for Africa (July 1992−June 1994), South America (1993), and Australia (1993). These fire-counts are determined from daily daytime data observed by NOAA polar orbiting satellites and processed into a GBT product of 1 km resolution. Fire-counts are reported when the 3.7 μm channel exceeds 320 K after screening for warm backgrounds, high clouds, high background reflectivity, Sun glint, and after visual inspection [*Arino and Melinotte*, 1995].

[7] Fire-count data products have some shortcomings. Clouds mask fires for ATSR and AVHRR. Cloud obscuration is less of a problem in tropical regions during the dry season when most burning takes place compared to boreal regions where cloud cover can persist for days [*Dwyer et al.*, 2000]. In algorithms for both ATSR and AVHRR, fire detection is expected even when the fire is smaller than the pixel size [*Dozier*, 1981], but the algorithms cannot detect multiple fires within a pixel, or differentiate subpixel fires of different sizes. Brush fires below a thick upper canopy will not be detected readily. The IGBP-DIS validation found the number of ATSR fire-counts is globally underestimated due mainly to nighttime detection, the relatively low temperature of boreal fires, cloud cover, and the 3-day return time [*Arino and Plummer*, 2001]. The main drawback with ATSR is the nighttime overpass, given that fire activity peaks in the afternoon due to both human activity and meteorological conditions [*Malingreau*, 1990]. Nighttime fire detection, however, reduces difficulties associated with daytime AVHRR observation such as Sun glint, warm surface detection, and high reflectivity surfaces. Despite their shortcomings, fire-counts provide the best current information on the seasonal and spatial variation of fire activity in many regions of the world.

[8] Figures 1a and 1b show respective composites of the available ATSR and AVHRR fire-counts, binned into $1° \times 1°$ boxes; note that the figures have different scales since AVHRR detects more fires than ATSR. Interannual variability also contributes to differences between the two products. Nearly all fire-counts are associated with biomass burning; however gas flares associated with the oil industry are seen readily in Figure 1a, for example, in the North Sea, Gulf of Mexico, Persian Gulf region, Nigeria and the Gulf of Guinea, northern Africa and northern Russia. A number of regions of intense and widespread biomass burning are apparent in the figure: Brazil, northern South America, Central America and Mexico, northern Africa (5−15°N), southern Africa (0−30°S), Australia, Indonesia and Malaysia, Southeast Asia, India, and the boreal forests of Asiatic Russia, Canada and Alaska.

2.2. TOMS AI Data Product

[9] *Hsu et al.* [1996] first demonstrated that TOMS data can be used to detect tropospheric UV-absorbing aerosols
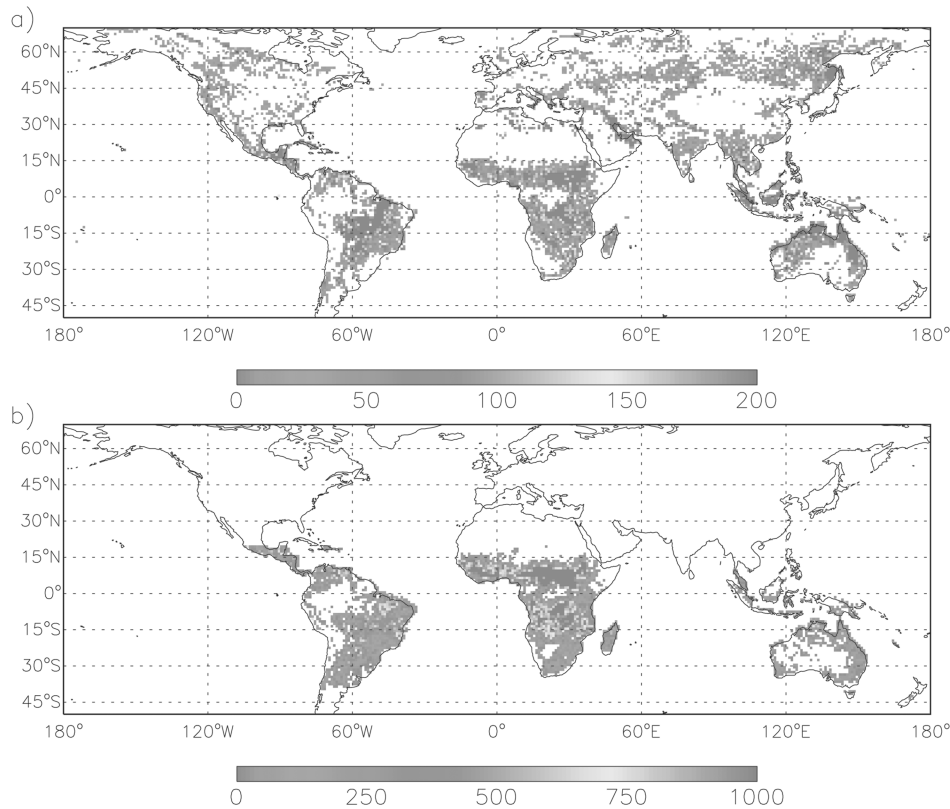
Figure 1. Fire-counts binned into $1° \times 1°$ grid boxes using the a) ATSR World Fire Atlas (August 1996 to December 2000) and b) AVHRR World Fire Atlas for Australia (1993), South America (1993), and Africa (July 1992 to June 1994). There was no AVHRR data available outside these three regions. See color version of this figure at back of this issue.

such as smoke. Aerosol information can be obtained over both land and water [*Herman et al.*, 1997; *Torres et al.*, 1998], and even snow and ice [*Hsu et al.*, 1999a]. The AI is a measure of the wavelength-dependent reduction of Rayleigh scattered radiance by aerosol absorption relative to a pure Rayleigh atmosphere [*Hsu et al.*, 1996; *Herman et al.*, 1997; *Torres et al.*, 1998]. It is often proportional to aerosol optical thickness [*Hsu et al.*, 1999b; *Chiapello et al.*, 2000]. The AI is defined as:

$$AI = -100\left(\log_{10}\left[(I_{\lambda 1}/I_{\lambda 2})_{\text{measured}}\right] - \log_{10}\left[(I_{\lambda 1}/I_{\lambda 2})_{\text{calculated}}\right]\right) \tag{1}$$

where I_{λ} is the backscattered radiance at wavelength, λ; $(I_{\lambda 1}/I_{\lambda 2})_{\text{measured}}$ is the ratio of backscattered radiances measured by TOMS; and $(I_{\lambda 1}/I_{\lambda 2})_{\text{calculated}}$ is the ratio calculated by a modified version of the Lambert equivalent reflectivity (LER) model for a pure Rayleigh atmosphere [*Dave*, 1978; *McPeters et al.*, 1996]. Backscattered radiances were measured by Nimbus-7 TOMS from November 1978 to May 1993 and by Earth-Probe TOMS from July 1996 to present. For Nimbus-7 TOMS $\lambda_1 = 340$ nm and $\lambda_2 = 380$ nm and for Earth-Probe TOMS $\lambda_1 = 331$ nm and $\lambda_2 = 360$ nm. These wavelength channels are not sensitive to ozone absorption. UV-absorbing aerosols such as desert dust, biomass burning smoke, and volcanic ash, dominate positive values of AI. Haze and volcanic sulfate aerosols dominate negative values. Nearly null values of AI can result from the presence of clouds or a mixture of absorbing and nonabsorbing aerosols. Clouds can reduce the amount of aerosols detected below them by obscuration, but they do not interfere with the detection of adjacent aerosols layers [*Herman et al.*, 1997]. The interference of the detection of aerosols by the presence of clouds should be at a minimum during the biomass burning season since it generally occurs during the dry season in the tropics. Conversely, this interference will be at a maximum during the rainy season when aerosol can be obscured by clouds and lost due to wet scavenging. Only positive values of AI corresponding to absorbing aerosols are considered in this study. Maps of monthly averaged AI for absorbing aerosols for July 1997 to June 1998 are presented in Figure 2. The major features of the monthly AI maps are discussed by region in section 4.2.

[10] A number of limitations associated with the TOMS AI data, as will be discussed in the following subsections, complicate its use in determining interannual variability of biomass burning emissions. When possible, we have adjusted the data to account for these observational problems.

2.2.1. Volcanic Eruptions

[11] There have been two major volcanic eruptions since 1979, El Chichón in Mexico on 4 April 1982 and Mt. Pinatubo in the Philippines on 15–16 June 1991. The Mt. Pinatubo eruption increased stratospheric aerosol loading nearly 30 times to 30 Tg [*McCormick and Veiga*, 1992], raising background levels of aerosol over the entire globe [*Thomason et al.*, 1997]. Aerosol loading remained well above background levels until early 1994 [*Fiocco et al.*,
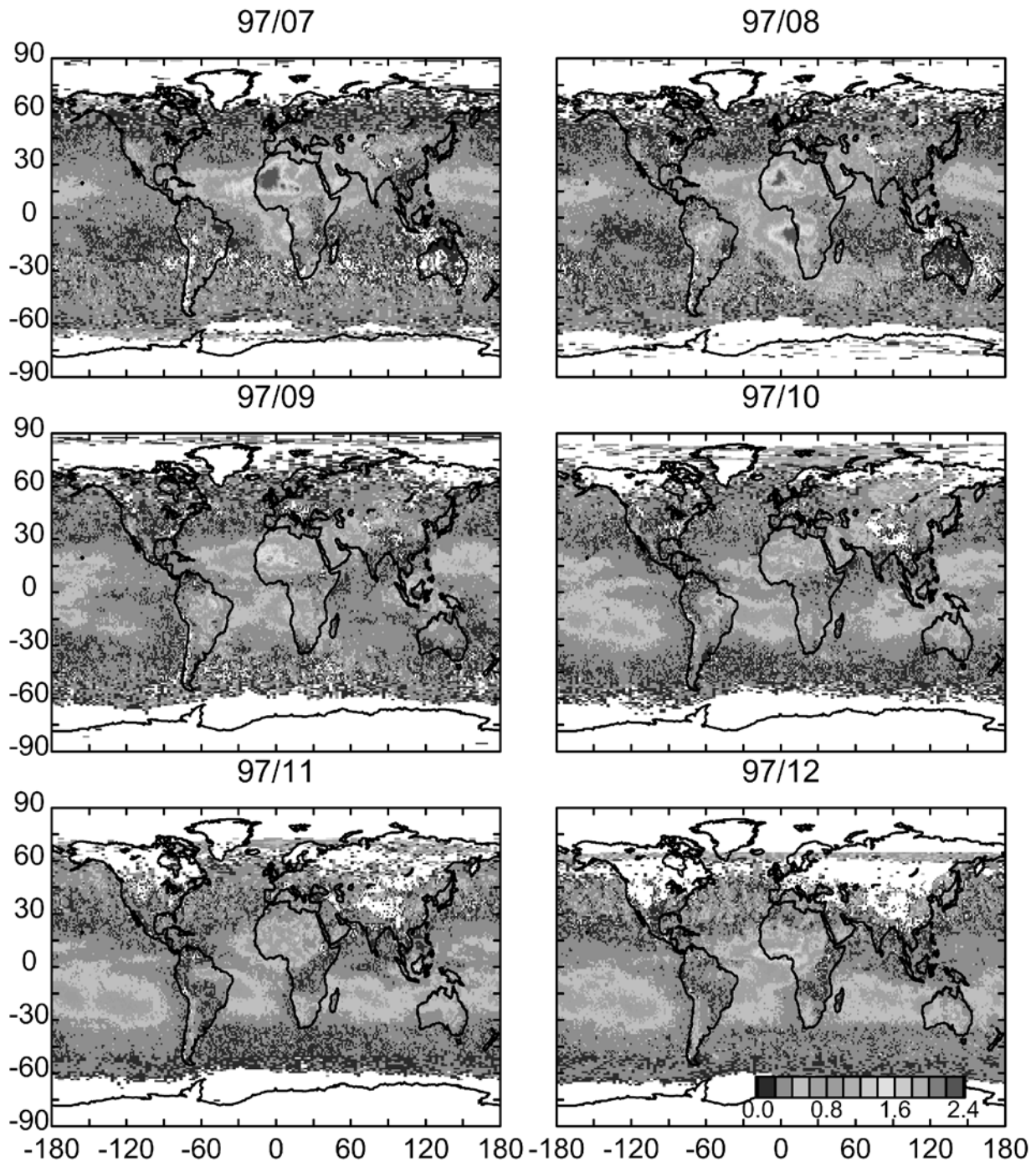
Figure 2. Monthly averaged AI as measured by TOMS for a complete year (i.e., July 1997 to June 1998). See color version of this figure at back of this issue.

1996]. The El Chichón eruption, while not as strong as the Mt. Pinatubo eruption, also increased background aerosol significantly [*DeLuisi et al.*, 1983]. We removed aerosol of volcanic origin by normalizing the posteruption data to data obtained prior to the eruptions. This will be discussed further in section 3.2.

2.2.2. Multiple Instruments and Missing Years

[12] A gap in AI data exists from May 1993 to July 1996. Although Meteor-3 TOMS was operational from August 1991 to November 1994, global AI data are not available due to its precessing orbit; the orbits of Nimbus 7 and Earth-Probe TOMS were Sun-synchronous [*Herman et al.*, 1997]. Data from the two TOMS instruments were normalized by multiplying AI from Nimbus 7 TOMS by 0.75 to compare it with Earth-Probe TOMS (O. Torres, private communication, 2000). Nimbus 7 TOMS is more sensitive to aerosol since AI is measured over 40 nm (340–380 nm) instead of 29 nm (331–360 nm) for Earth-Probe TOMS.
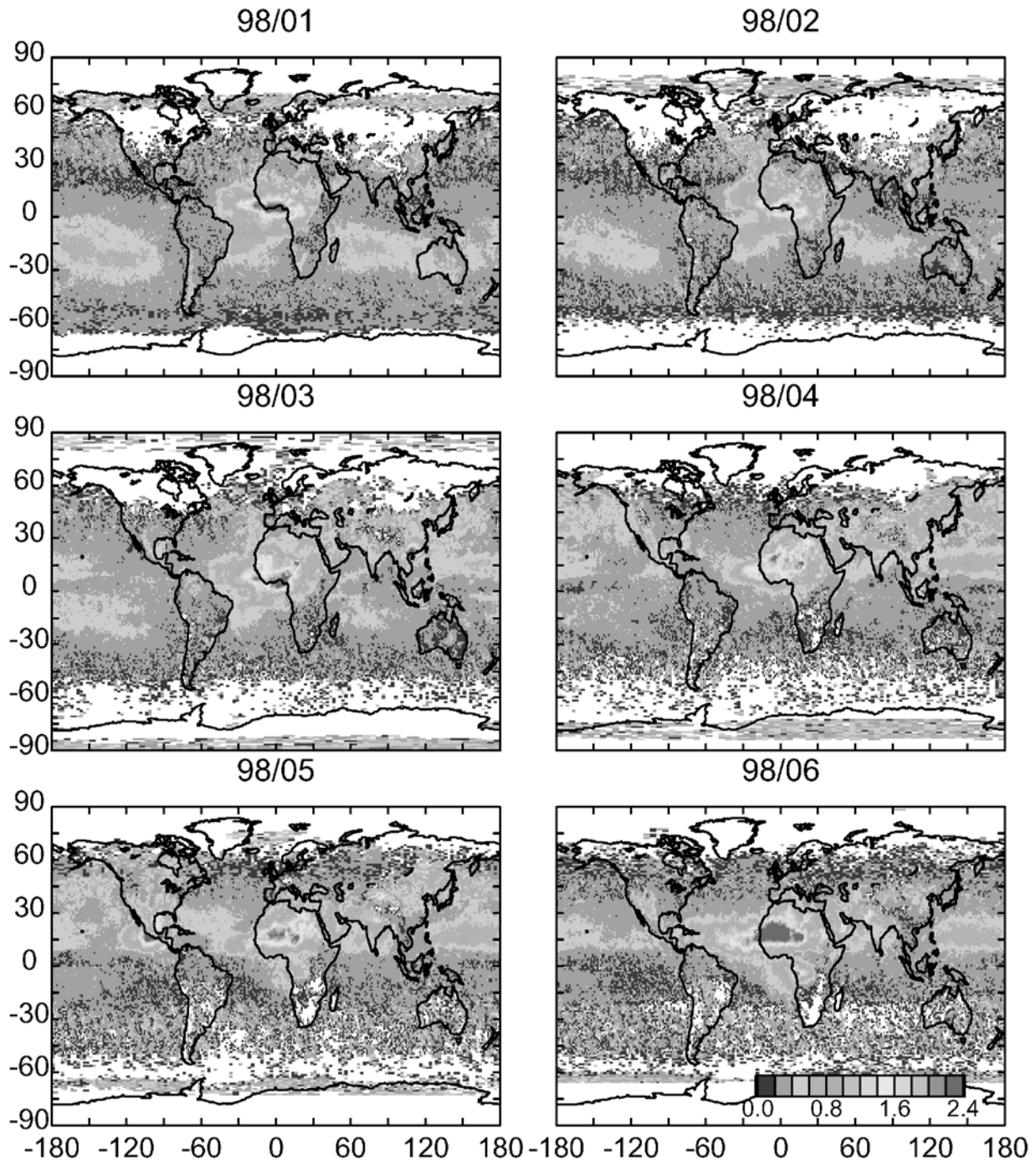
Figure 2. (continued)

2.2.3. Altitude Dependency

[13] Values of the AI are sensitive to the altitude of the aerosol layer [*Herman et al.*, 1997; *Torres et al.*, 1998]. The TOMS instrument is generally more sensitive to aerosol at higher altitudes than near the surface, since the mean height of backscattered UV radiation is above the boundary layer [*Herman et al.*, 1997; *Torres et al.*, 1998; *Hsu et al.*, 1999b]. This altitude dependence can be removed if aerosol type and height of the aerosol plume are known. We did not attempt to correct for plume height, as this would require an analysis beyond the scope of this study. Our inherent assumption is that the height of aerosols in a given region does not vary significantly from year to year. *Hsu et al.* [1999b] showed that the TOMS aerosol optical thickness (AOT) for biomass burning smoke and dust is linearly proportional to the Sun photometer AOT obtained from the Aerosol Robotic Network (AERONET). They concluded that the aerosol properties and layer heights likely varied little from year to year
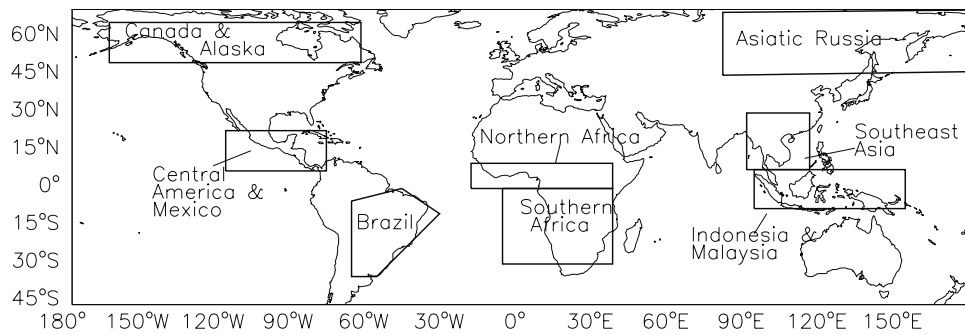
Figure 3. Regions for which $MRAI_{m,n}$ is estimated.

since the proportionalities were reproducible for several years. They also found that these linear proportionalities were dissimilar for biomass burning over Africa and over South America due to differing types of aerosols and typical aerosol layer heights. Consequently we examine interannual variability for specific regions, and we do not compare AI values from one region to another. We show in section 4.2 that AI data are consistent with other measures of variability in biomass burning.

[14] We are not able to use AI as a surrogate for biomass burning in some regions since smoke in the boundary layer may not be represented reliably in the data. For example, smoke plumes from low-intensity fires, such as leaf-litter, savanna grass, and peat fires, generally do not generate their own convection and may not rise out of the boundary layer [*Rapalee et al.*, 1998; *Levine*, 1999; *Muraleedharan et al.*, 2000]. This problem becomes especially important over Africa where much of the aerosol is trapped in the boundary layer and is not readily detected by the TOMS satellite until the aerosol is transported over the Atlantic ocean, as will be discussed in sections 4.2.5 and 4.2.6 (e.g., Figure 2, August and September). Persistent stable layers hamper vertical transport over land in this region during the dry season. *Stocks et al.* [1996] report convection column heights generally below 3 km from fires on an arid savanna in southern Africa, and observations over southern Africa and the eastern Atlantic show that aerosols and gases such as CO are elevated below 3–4 km [*Browell et al.*, 1996; *Garstang et al.*, 1996].

[15] At the other extreme, regions with hotter burning forest fires may be more apparent in the AI data. These fires are likely to generate their own convection because of the large amount of biomass available, injecting trace gas emissions high into the troposphere [*Cofer et al.*, 1996a; *Levine*, 1999; *Matsueda et al.*, 1999; *Fromm et al.*, 2000; *Kita et al.*, 2000].

2.2.4. Aerosol Contamination

[16] Desert dust is a seasonal, and often persistent, contributor to tropospheric aerosol loading for several regions of the world [*Prospero and Carson*, 1972; *Ginoux et al.*, 2001]. Dust sources are easily identified with AI data [*Herman et al.*, 1997; *Chiapello et al.*, 1999]. Major sources include the deserts of northern Africa, the Middle East, China and Mongolia, and dry or seasonally dry lake and riverbeds, such as near Lake Chad in Africa, the Aral Sea, and Lake Eyre in Australia [*Herman et al.*, 1997].

[17] Aerosol from both deserts and biomass burning are transported away from their source regions enhancing back-

ground aerosol a considerable distance downwind. This can be seen in Figure 2 during the peak desert dust season in Africa; the AI is elevated in the entire zonal band ($0–30°N$) in June, July and August. A similar enhanced zonal band ($0–30°S$) of aerosol south of the equator is seen from September to December during that hemisphere's burning season. The magnitude of this enhancement in background AI is much smaller than the regional signal when biomass burning occurs, and, therefore, does not contribute substantially to the total regional aerosol.

2.2.5. Aerosol Removal and Transport

[18] Meteorology affects both the rate of aerosol transport away from its source and the rate of aerosol deposition. A smoke plume exported from a source region quickly, or one removed through precipitation, will reduce the AI signal for a region more rapidly than a slowly dispersing plume. As mentioned earlier, most biomass burning occurs during the dry season, so aerosol washout is at a minimum. We analyze interannual variability in the AI for large regions to allow for the drift of the aerosol from its sources, and for the decrease in TOMS sensitivity near the surface. These regions are shown in Figure 3.

2.2.6. TOMS Instrumental Drift

[19] *Herman et al.* [1997] reported a small instrumental drift for Nimbus 7 TOMS beginning in 1990. Because of this error, small trends detected in the AI may not be reliable between 1990 and 1993. Unfortunately, this instrumental drift coincided roughly with the eruption of Mt. Pinatubo and a prolonged ENSO event. We do not correct for the instrumental drift error and assume the signal from this error is small relative to the signals from biomass burning aerosol and volcanic aerosol from the eruption of Mt. Pinatubo.

2.2.7. Spatial Extent of Data Coverage

[20] The orbits and scans of the TOMS instruments were designed to provide contiguous coverage of the globe, but AI data are lacking in regions of cloud obscuration [*Herman et al.*, 1997]. We avoid data quality issues for TOMS when measurements are taken at high solar zenith angles [*Hsu et al.*, 1999b] by using data only from late spring to early fall for high latitudes ($>±60°$). Forest fires usually occur during this period in boreal regions [*Skinner et al.*, 2000].

2.3. Climatological Annual Biomass Burned Inventory

[21] In this study, we use an inventory of the total annual biomass burned developed by J. A. Logan and R. Yevich as summarized by *Lobert et al.* [1999]; however, our method of determining seasonal and interannual variation of biomass burned can be applied to other inventories. Catego-

Table 1. Emission Factors[a] Applied to Total Biomass Burned Inventory of J. A. Logan and R. Yevich

Biomass Type	Range[b] of EFs, g CO/kg DM	EF[c], g CO/kg DM
Savanna/Grassland	45–80[d]	65
Forests[e]		
Tropical	47–152[f]	100
Extratropical	44–158[g]	97
Boreal	70–120[h,i]: 135–350[i,j]	120
Agricultural Residues[k]	29–143[l]	51[m]

[a]Emission factor is expressed as g CO/kg DM; DM = dry matter.
[b]Range of emission factors (EFs) in the literature.
[c]Average EF used in this work.
[d]*Andreae et al.* [1996], *Sholes et al.* [1996], *Cofer et al.* [1996b], *Delmas et al.* [1995], *Lacaux et al.* [1995], *Hurst et al.* [1994a, 1994b], and *Ferek et al.* [1998].
[e]EFs used for forest fires, deforestation, and shifting cultivation activities.
[f]*Ferek et al.* [1998], *Ward et al.* [1991], *Kaufman et al.* [1992], and *Ward et al.* [1992].
[g]*Laursen et al.* [1992], *Hegg et al.* [1990], *Radke et al.* [1991], *Sussot et al.* [1990], and *Ward and Hardy* [1991].
[h]Flaming stage.
[i]*Cofer et al.* [1998].
[j]Smoldering stage.
[k]Agricultural residues burned in the field.
[l]EFs for specific residues from *Yevich and Logan* [2002].
[m]Weighted average EF as recommended by *Yevich and Logan* [2002].

Table 2. Annual Mean Emissions for Various Regions of the Globe

Region	Emissions, Tg CO yr^{-1}
Globe (90°N–90°S)	437
Tropics (30°N–40°S)	398
Southern Hemisphere	188
Southern Africa	86
Brazil	60
Indonesia and Malaysia	36
Northern Hemisphere (0–30°N)	210
Southeast Asia	82
Northern Africa	87
Central America and Mexico	9
Northern South America	15

ries of biomass burning in the inventory are deforestation, shifting cultivation, agricultural residues burned in the field, savanna burning, and forest wild fires. The inventory is not representative of one individual year since it incorporates input data from many sources from 1980 to the early 1990s, including deforestation data for 1981–1990 [*FAO*, 1993]. The inventory of Logan and Yevich is compared to other estimates of biomass burning by *Lobert et al.* [1999]. We converted the annual biomass burned into an emissions inventory for CO by applying emission factors (g CO emitted/kg DM burned; DM = dry matter) for each of the specific categories of biomass burned (Table 1). These emission factors are similar to those recommend in a recent critical review by *Andreae and*

Merlet [2001], except for two modifications. First, we use a somewhat higher emission factor for boreal forests compared to other extratropical forests, following *Cofer et al.* [1998]. Second, we use emission factors recommended by *Yevich and Logan* [2002] for agricultural residues burned in the field. The spatial distribution of annual CO emissions from all categories of biomass burning is presented in Figure 4. Annual total CO emissions by region are shown in Table 2. Global CO emissions total 437 Tg yr^{-1} with the majority occurring in tropical regions. This total does not include CO derived from the combustion of biofuels or from the oxidation of nonmethane hydrocarbons (NMHC) emitted concurrently with CO during biomass burning activities.

3. Methods Used to Estimate Seasonal and Interannual Variability

3.1. Average Seasonal Variation of Biomass Burning

[22] We estimate average monthly biomass burning emissions for 1° × 1° gridboxes using an annual biomass burned inventory and monthly total fire-count data. Four complete years of ATSR and 1–2 years of AVHRR observations were available. Our results will be improved as more years of fire-count data become available.

[23] First, we summed the total number of fires reported by each data record, $N_{k,m}^{ATSR}$ and $N_{k,m}^{AVHRR}$, occurring within
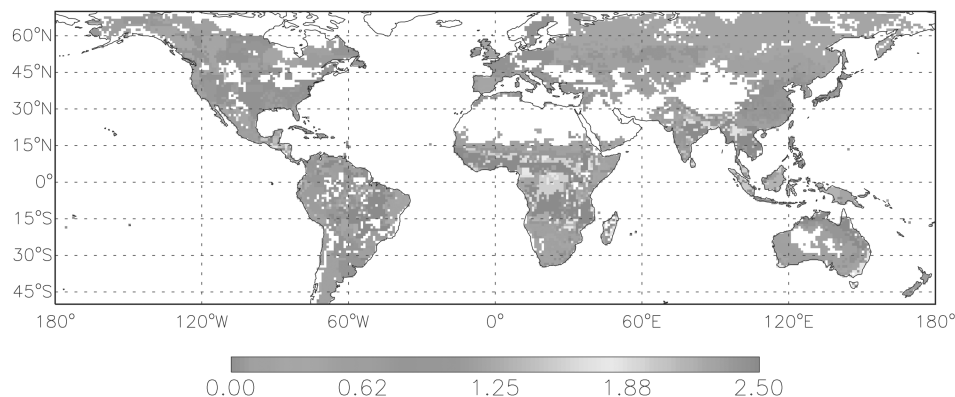

Figure 4. Spatial distribution of mean CO emissions from biomass burning ($\times$ 10^{19} molecules CO cm^{-2} yr^{-1}). There are data points higher than 2.5 × 10^{19} molecules CO cm^{-2} yr^{-1}, however, for clarity, the scale is capped. See color version of this figure at back of this issue.
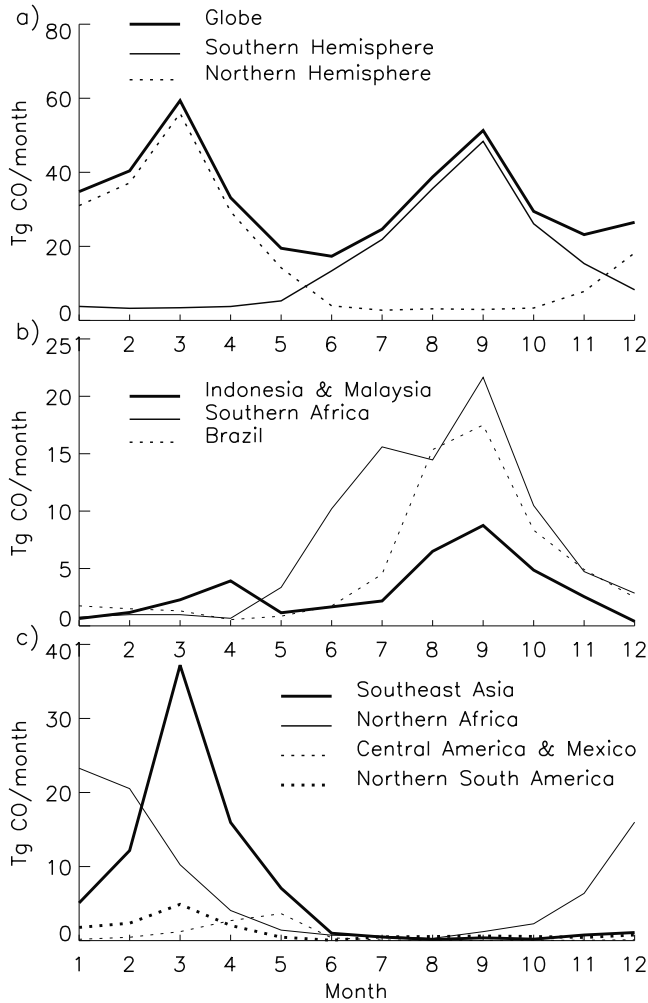
Figure 5. Average biomass burning emission rate (Tg CO month^{-1}) for the a) globe, Northern Hemisphere, and Southern Hemisphere, b) Indonesia and Malaysia, Brazil, and southern Africa, and c) Southeast Asia, northern Africa, Central America and Mexico, and northern South America.

each $1° \times 1°$ gridbox, k, for each month, m, over the time period of observations. $M_{k,m}$ is the number of months of ATSR observations, four in our case. Thus, $N_{k,8}^{ATSR}$ is the total sum of fire-counts in four Augusts. Then, we determined the fraction of annual biomass burning emissions occurring in each month for each grid box for both ATSR, $F_{k,m}^{ATSR}$, and AVHRR, $F_{k,m}^{AVHRR}$, with respect to the total for all months:

$$F_{k,m}^{ATSR} = \frac{N_{k,m}^{ATSR}}{\sum_{m=1}^{12} N_{k,m}^{ATSR}} \tag{2}$$

$$F_{k,m}^{AVHRR} = \frac{N_{k,m}^{AVHRR}}{\sum_{m=1}^{12} N_{k,m}^{AVHRR}} \tag{3}$$

We combined the two, weighting by $M_{k,m}$ to calculate the fraction of burning that occurs each month, $F_{k,m}$:

$$F_{k,m} = \frac{M_{k,m}^{ATSR} * F_{k,m}^{ATSR} + M_{k,m}^{AVHRR} * F_{k,m}^{AVHRR}}{M_{k,m}^{ATSR} + M_{k,m}^{AVHRR}}. \tag{4}$$

The average monthly emissions, $E_{k,m}$, are calculated by

$$E_{k,m} = F_{k,m} * C_k \tag{5}$$

where C_k is the annual emissions from the biomass burning inventory in the grid box. This method preserves the total emissions, even though fire-counts are underestimated as discussed in section 2.1.

[24] Fire-counts were not used to determine the seasonal variation of biomass burning emissions poleward of $\pm 40°$ due to the relative sparseness of fires in this region and the large spatial interannual variability on a timescale of decades. Poleward of $\pm 40°$ the seasonal variation of emissions is based on statistics for the areas of fires.

[25] The resulting seasonal variation in biomass burning emissions is presented in Figures 5 and 6and is discussed in section 4.1. Although fire-counts were evident in oil producing regions such as eastern Saudi Arabia (Figure 1a), they do not affect the monthly sums in Figures 5 and 6 since most gas flares occur in regions where the annual emissions from biomass burning is very low or zero (e.g., around and in the Persian Gulf). Our seasonal variation is consistent with the seasonal variation determined from AVHRR fire-counts by *Cooke et al.* [1996] and *Justice et al.* [1996] over Africa.

3.2. Long-Term Interannual Variation of Biomass Burning (1979–2000)—TOMS AI

[26] The TOMS AI data product was used to estimate the interannual variability of biomass burning for the regions presented in Figure 3. We illustrate the method of processing the data using the Indonesia and Malaysia region as an example (Figure 7).

[27] First, we multiplied AI from Nimbus 7 TOMS by 0.75 to normalize it with Earth-Probe TOMS as discussed in section 2.2.2. Two months of data, July and August 1990, were removed because of apparent data quality problems. We processed only positive values of AI data, corresponding to absorbing aerosols, creating a monthly mean value of the AI, $MAI_{k,m,n}$, for each $1° \times 1.25°$ grid box, k, for each month, m, of each year, n. The resolution of the AI data is $1° \times 1.25°$. For each month, we used the total number of days of available data, $NAI_{k,m,n}$; there are often missing data due to cloud obscuration as discussed in section 2.2.7. To create a mean AI for each region, we summed over the number of boxes within a region, $kmax$, the product of $MAI_{k,m,n}$ and $NAI_{k,m,n}$ and divided by the sum of $NAI_{k,m,n}$. We call this value the Monthly Regional AI ($MRAI_{m,n}$):

$$MRAI_{m,n} = \frac{\sum_{k=1}^{kmax} \left(MAI_{k,m,n} * NAI_{k,m,n} \right)}{\sum_{k=1}^{kmax} NAI_{k,m,n}}. \tag{6}$$

Figures 7a–7c illustrates, respectively, $\sum_{k=1}^{kmax} MAI_{k,m,n}$, $\sum_{k=1}^{kmax} NAI_{k,m,n}$, and $MRAI_{m,n}$ as a function of time for the Indonesia and
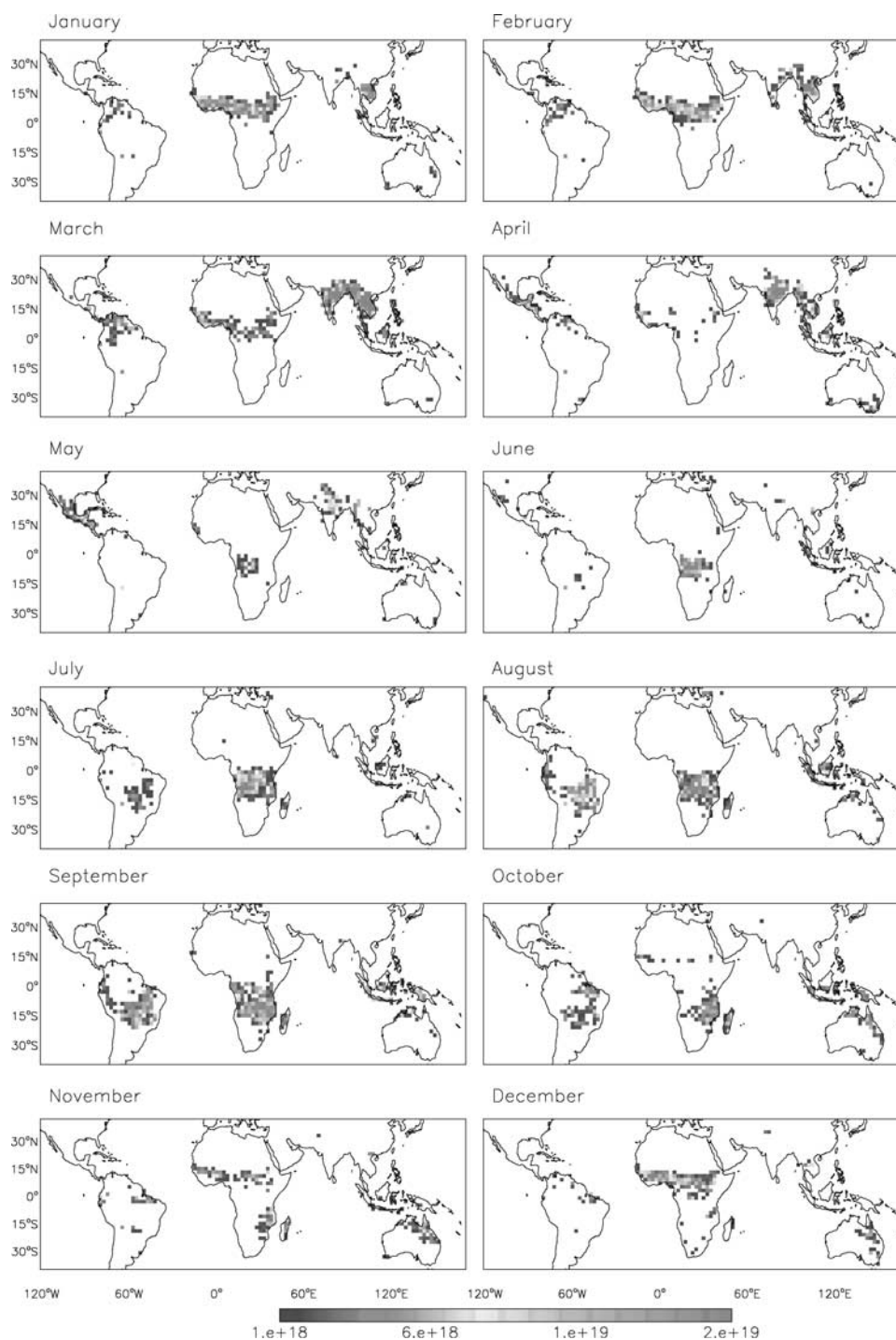
Figure 6. Mean seasonal variation in biomass burning emissions (molecules CO cm^{-2} month^{-1}). See color version of this figure at back of this issue.

Malaysia region. $NAI_{k,m,n}$ was elevated during the time of the ENSO events of 1982–1983 and the early 1990s, due to less cloud cover during the drought conditions and higher aerosol loads from drought-enhanced fires. Excluding the time period of the two ENSO events, there appears to be an upward trend in the $NAI_{k,m,n}$ over the period of observations of Nimbus 7 TOMS.

[28] We removed background $MRAI_{m,n}$ for each region by subtracting the value of $MRAI_{m,n}$ when no burning occurs (i.e., the annual minimum) for that particular region. For all

regions except Indonesia and Malaysia a constant background was subtracted because the annual minima varies little over the entire data record. Interestingly, the seasonal minimum increased with time for Indonesia and Malaysia (Figure 7c). This suggests background aerosol in this region has been increasing over the last two decades, possibly from increased rates of biofuels use and deforestation [*Brauer and Hisham-Hashim*, 1998]. We removed the background for this region by fitting a straight line through the annual minima and subtracting the background for each year according to the
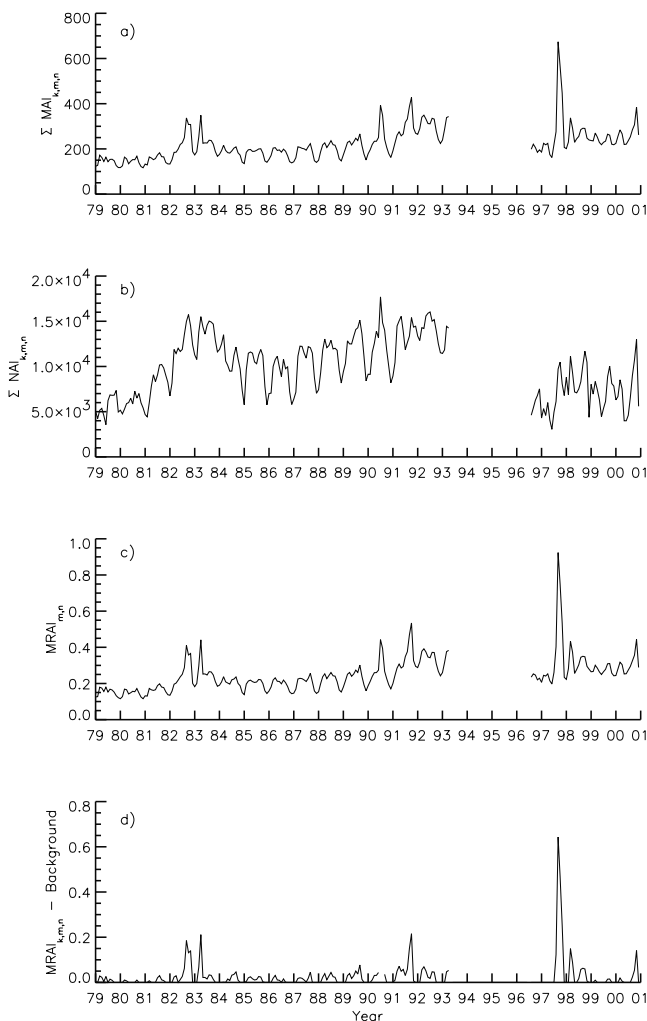
Figure 7. Steps in processing AI data for the Indonesia and Malaysia region: a) $\sum_{k=1}^{kmax} MAI_{k,m,n}$ (relative units) after AI from Nimbus 7 TOMS is normalized to Earth-Probe TOMS, b) $\sum_{k=1}^{kmax} NAI_{k,m,n}$ (number of days), and c) $MRAI_{m,n}$ (relative units) before background removal, and d) $MRAI_{m,n}$ (relative units) with background and volcanic contamination removed.

slope of the line, with results shown in Figure 7d; in doing so, we omitted data for a period of two years after the eruptions of El Chichón and Mt. Pinatubo, as the background $MRAI_{m,n}$ was elevated. For some regions, this elevated background was obvious in the data for several years, especially the tropics. As a second step, we removed the elevated background due to aerosol of volcanic origin by normalizing the annual minimum to years prior to the eruptions. The eruptions of both volcanoes occurred during major ENSO-enhanced burning events. Thus the removal of a background due to volcanic aerosol is rather subjective for Indonesia and Malaysia, which typically experience enhanced fire activity during ENSO events.

[29] The resulting $MRAI_{m,n}$ for the eight regions in Figure 3 are shown in Figure 8. As will be discussed in section 4.2, the $MRAI_{m,n}$ performs well as a surrogate for biomass burning in all regions except northern and southern Africa. For Asiatic Russia and Canada and Alaska, we do

not plot $MRAI_{m,n}$ in the winter as discussed in section 2.2.7. Aerosol contamination from outside the regions is seen for northern Africa, southern Africa, and Central America and Mexico, in seasons when biomass burning is not occurring within these regions. For northern Africa, desert dust from the Sahara contaminates the TOMS AI signal during the summer months; this is seen in Figure 8g as a secondary peak. Biomass burning aerosol from the northern Africa region is transported into the southern Africa region, and is seen as a small peak around January in Figure 8h. The Central America and Mexico region is contaminated by desert dust from the Sahara in summer (Figure 8e). This issue of contamination of regions will be discussed in further detail in section 4.2.

[30] The $MRAI_{m,n}$ is not comparable among regions, as discussed in section 2.2.3, so that the same value for two regions does not mean that there is the same amount of aerosol present over each. For example, an $MRAI_{m,n}$ of 1.2 for Brazil does not necessarily mean that a greater quantity of aerosol is present than an $MRAI_{m,n}$ equal 1.0 for Indonesia. For each region, $MRAI_{m,n}$ is dependent on a number of factors discussed in section 2.2 such as the height of the aerosol layer, the aerosol type, and the intensity of the burning event, as well as by the quantity of background AI removed.

[31] We calculated emissions, $E_{m,n}$, adjusted by $MRAI_{m,n}$ of a trace gas for each month, m, and year, n, for each region:

$$ E_{m,n} = C_{reg} \left(\frac{MRAI_{m,n}}{\frac{1}{N} \sum_{1}^{N} \sum_{m=1}^{12} MRAI_{m,n}} \right) \qquad (7) $$

where the denominator is the annual mean MRAI for that region, N is the number of years of observations, and C_{reg} is the sum of annual biomass burning emissions from the base inventory over $kmax$ boxes within the region. The assumption is made that the base inventory represents the average biomass burning emissions over the two decades of the AI data record. The accuracy of the time-dependent emission inventory developed here depends, of course, on the accuracy of the base inventory, as well as on the method used for estimating interannual variability.

[32] The $MRAI_{m,n}$ is only a regional proxy of interannual variability because aerosol can drift from its source and is subject to deposition as discussed in section 2.2.5. Therefore, while $E_{m,n}$ varies for a region for any given month as compared to the base emission inventory, the spatial pattern of emissions within the region is the same as that in the base inventory. In section 3.3 we present a method to use the ATSR fire-counts for August 1996 to July 2000 to redistribute the emissions within the region according to the locations of the fire-counts each month.

[33] We filled in the TOMS data gap (mid-1993 to mid-1996) as much as possible with other sources of information on burning. Annual total area burned (TAB_n) statistics for Indonesia, Russia, Canada, and Alaska are available, although the statistics from Russia and Indonesia are of questionable quality [Kasischke et al., 1999; Mori, 2000]. Consequently, we used literature reports to fill in the data
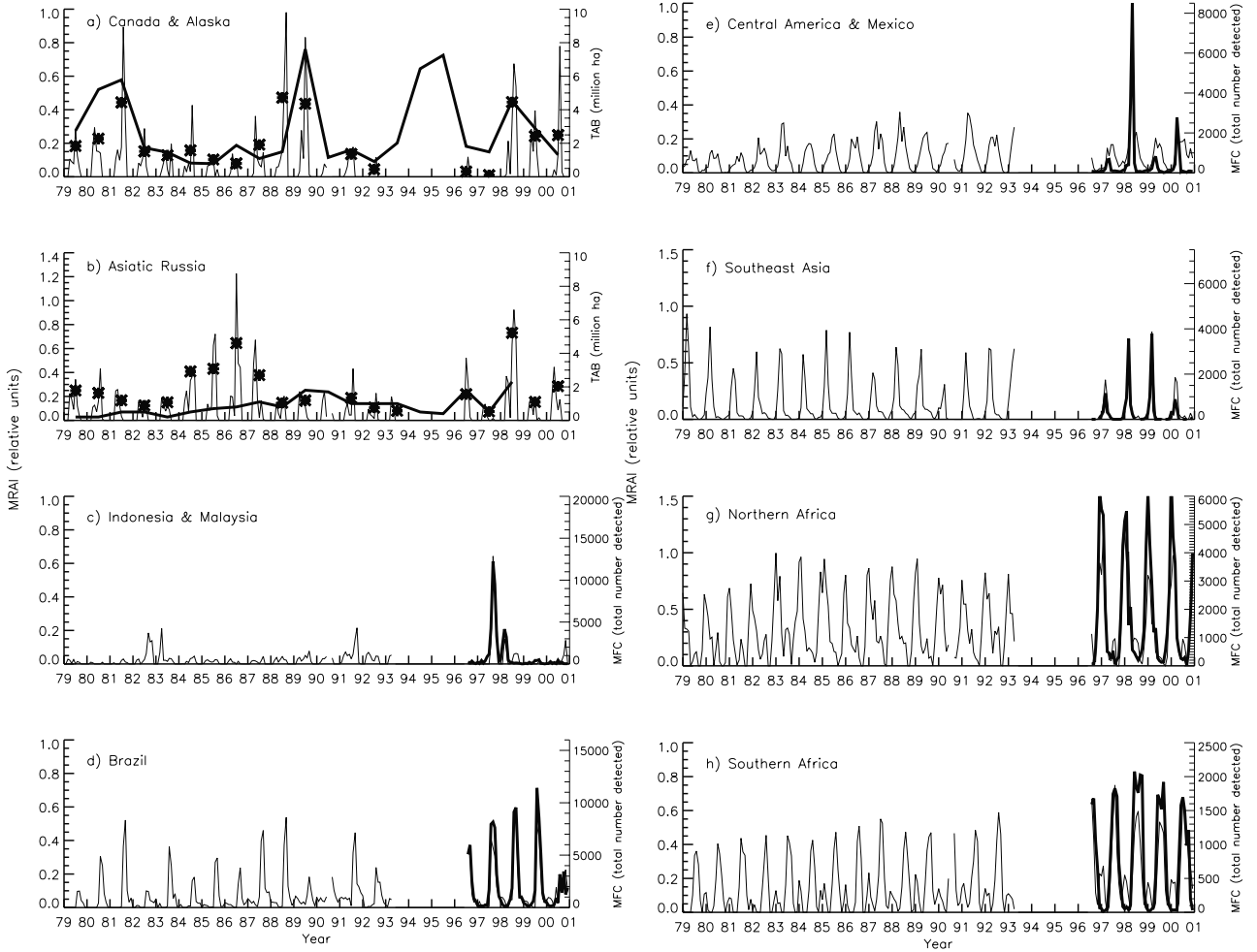
Figure 8. $\text{MRAI}_{m,n}$ (relative units) as a function of time (1979–2000) for a) North America (Canada and Alaska), b) Asiatic Russia, c) Indonesia and Malaysia, d) Brazil, e) northern Africa, f) southern Africa, g) Central America and Mexico, and h) Southeast Asia. $\text{MRAI}_{m,n}$ is presented as a fine solid line. For a) and b) *TAB* (million ha yr^{-1}) as reported by government agencies is presented as a heavy solid line. The star (*) represents *ITA* for a summer season. For c–h) *MRF* (total regional number) from August 1996 to December 2000 is presented as a heavy solid line.

gap for Indonesia as discussed in section 4.2.1. For Canada and Alaska we used TAB_n to estimate $\text{MRAI}_{m,n}$ for the TOMS data gap according to the following equation:

$$\text{MRAI}_{m,n} = \left(\frac{TAB_n}{\overline{TAB}}\right)\overline{\text{MRAI}_m} \qquad (8)$$

where $\overline{TAB}$ is the mean of TAB_n and $\overline{\text{MRAI}_m}$ is the mean value of $\text{MRAI}_{m,n}$ for 1979–2000 excluding 1993–1996. Equation (8) assumes that there is a close correlation between TAB_n and the regional AI, $\text{MRAI}_{m,n}$, averaged over a year; this issue will be discussed in section 4.2.7.

[34] For areas outside the regions shown in Figure 3, we did not estimate interannual variations of biomass burning. Instead we applied the mean seasonal variation (section 3.1) to the mean biomass burned inventory.

3.3. Increased Spatial and Temporal Resolution of Interannual Variability of Biomass Burning (August 1996 Through July 2000)

[35] The ATSR fire-counts provide additional information about the location of fires and the interannual variability of

biomass burning from August 1996 to July 2000. We implemented three different approaches for using the ATSR data.

1. For regions where the $\text{MRAI}_{m,n}$ was not estimated or found to be a poor surrogate of biomass burning (e.g., Africa as is discussed in section 4.2), interannual variability was determined from the ATSR data for August 1996 to July 2000. Following a similar approach to the seasonal variation calculation (section 3.1), we determined emissions $E_{k,m,n}$, for each grid box from the number of fire-counts, $N_{k,m,n}^{ATSR}$, for each month, m, of each year, n, with respect to monthly mean fire-counts:

$$E_{k,m,n} = C_k \left(\frac{N_{k,m,n}^{ATSR}}{\frac{1}{4}\sum_{n=1}^{4}\sum_{m=1}^{12} N_{k,m,n}^{ATSR}}\right) \qquad (9)$$

where C_k is the annual mean emissions in gridbox, k, from the base inventory. The factor of 1/4 arises from the number

Table 3. Ratio of the Mean $\overline{\mathrm{MRAI}}_{4\mathrm{year}}$ From August 1996 to July 2000 to the Mean $\overline{\mathrm{MRAI}}$

Region	Ratio
Indonesia and Malaysia	2.4
Brazil	1.3
Central America	1.2
Canada and Alaska	1.2
Asiatic Russia	1.3
Southeast Asia	0.8

of years in the calculation. Equation (9) assumes the average emissions calculated from the four years of ATSR fire-count data in each $1° \times 1°$ grid from August 1996 through July 2000 are represented by the average emissions of the base inventory. We defaulted to the seasonal variation determined from wildfire statistics in the few high latitude boxes where there are no ATSR fire-count data. Because of the limited temporal extent of the fire-count data, $E_{k,m,n}$ should be reevaluated as additional fire-count data become available.

The TOMS AI provides an indication of how representative these four years are with respect to a long-term record. Table 3 contains the ratio of the mean $\mathrm{MRAI}_{m,n}$ over the four years of fire-counts, $\overline{\mathrm{MRAI}}_{4\mathrm{year}}$, to the mean of all $\mathrm{MRAI}_{m,n}$ for the entire data record (1979–2000), $\overline{\mathrm{MRAI}}$, for regions in which $\mathrm{MRAI}_{m,n}$ agreed well with fire-counts as discussed in section 4.2. For Indonesia and Malaysia $\overline{\mathrm{MRAI}}_{4\mathrm{year}}$ was 2.4 times larger than the $\overline{\mathrm{MRAI}}$ due to emissions during the El Niño of 1997–1998. In other regions, $\overline{\mathrm{MRAI}}_{4\mathrm{year}}$ is within 30% of $\overline{\mathrm{MRAI}}$.

2. For the regions of Brazil, Central America, and Southeast Asia (Figure 3), we combine ATSR fire-counts and the TOMS AI such that we use the higher spatial resolution of the fire-counts, but correct the ATSR temporal bias with the AI data. We correct this bias by scaling the emissions from each region by the values in Table 3. We perform the same calculation as in equation (9), but assume here that the mean biomass burned during the TOMS record (1979–2000) for each region is represented by the mean emission inventory. We multiply $E_{k,m,n}$ in each $1° \times 1°$ grid box, k, by the values in Table 3 for the appropriate region:

$$E_{k,m,n} = C_k \left(\frac{\overline{\mathrm{MRAI}}_{4\mathrm{year}}}{\overline{\mathrm{MRAI}}} \right) \left(\frac{N_{k,m,n}^{ATSR}}{\frac{1}{4} \sum_{n=1}^{4} \sum_{m=1}^{12} N_{k,m,n}^{ATSR}} \right). \quad (10)$$

3. For the Canada and Alaska, Asiatic Russia, and Indonesia and Malaysia regions (Figure 3), ATSR fire-count data show dramatic spatial variability from year to year. We assume the base inventory represents average emissions for each region, rather than for each $1° \times 1°$ grid. We use fire-counts to distribute total monthly regional emissions, $E_{m,n}$ (equation (7)) within each region. Interannual variability in total regional emissions, determined from $\mathrm{MRAI}_{m,n}$, is used to scale monthly average emissions by region.

$$E_{k,m,n} = E_{m,n} \left(\frac{N_{k,m,n}^{ATSR}}{\sum_{k=1}^{kmax} N_{k,m,n}^{ATSR}} \right). \quad (11)$$

[36] Table 4 contains the resultant monthly emissions for CO determined from equations (9)–(11). The time period of ATSR fire-count data is interesting because of the number of large biomass burning events that took place in a number of regions: Asiatic Russia (summer 1998), Canada and Alaska (summer 1998), Mexico and Central America (May 1998), and Indonesia and Malaysia (September and October 1997; March 1998). Above average monthly emissions can be seen in Table 4 during these events.

[37] Figure 9 illustrates the interannual variation for April and August. Substantial interannual variability occurs in all months except January and December. Emissions in India are much higher during April 1999 than either 1997 or 1998 (Figures 9a–9c). Emissions are much higher in Central America and Mexico during April 1998 than in either April 1997 or 1999. Global emissions for April 1998 and 1999 were similar (Table 4) despite the spatial interannual variability. For the month of August, there is modest interannual variability in the emissions in Brazil and Indonesia and Malaysia, but more remarkable is the spatial variability in the boreal forests (Figures 9d–9f). Large fires are evident in the western part of the region during August 1997, in contrast with fires in the far east of Russia along the Sea of Okhotsk during August 1996 and 1998. Rather than applying uniform emissions across Asiatic Russia as in Figure 4, equation (11) distributes emissions according to fire-counts.

4. Results

4.1. Mean Seasonal Variation

[38] Biomass burning is occurring in some region of the world at all times of the year, but peaks in March and again in September on a global scale (Figures 5a and 6). The peak in December to April during the Northern Hemisphere dry season is associated predominately with burning in the tropical regions of northern Africa and Southeast Asia, with much smaller contributions from Central America and Mexico and northern South America (Figure 5c). The peak in August to October during the Southern Hemisphere dry season is associated with burning in southern Africa and Brazil, with smaller contributions from Indonesia and Malaysia (Figure 5b). Although the Indonesia and Malaysia region straddles the equator, the burning season generally occurs in the latter half of the year (Figure 5b). Of the total

Table 4. Interannual Monthly Variation in Global CO Emissions From Biomass Burning as Determined From Fire-Counts and AI[a]

|	Annual Average	1996	1997	1998	1999	2000
January	35.0		29.0	36.9	32.6	32.8
February	40.3		43.6	48.0	38.2	35.1
March	59.2		45.8	69.2	67.8	40.0
April	37.9		15.0	44.7	40.5	38.5
May	23.8		20.1	45.5	23.7	27.9
June	24.1		18.1	26.0	19.5	20.6
July	34.5		27.4	49.7	33.1	27.7
August	47.1	48.3	59.3	82.6	50.6	
September	54.2	46.2	105.9	75.1	49.8	
October	33.2	21.5	77.4	44.5	42.7	
November	22.2	23.8	45.0	18.9	12.8	
December	25.6	29.3	23.9	24.2	17.2	
Total	437	169	511	565	429	223

[a]Global CO emission is expressed as Tg/month.
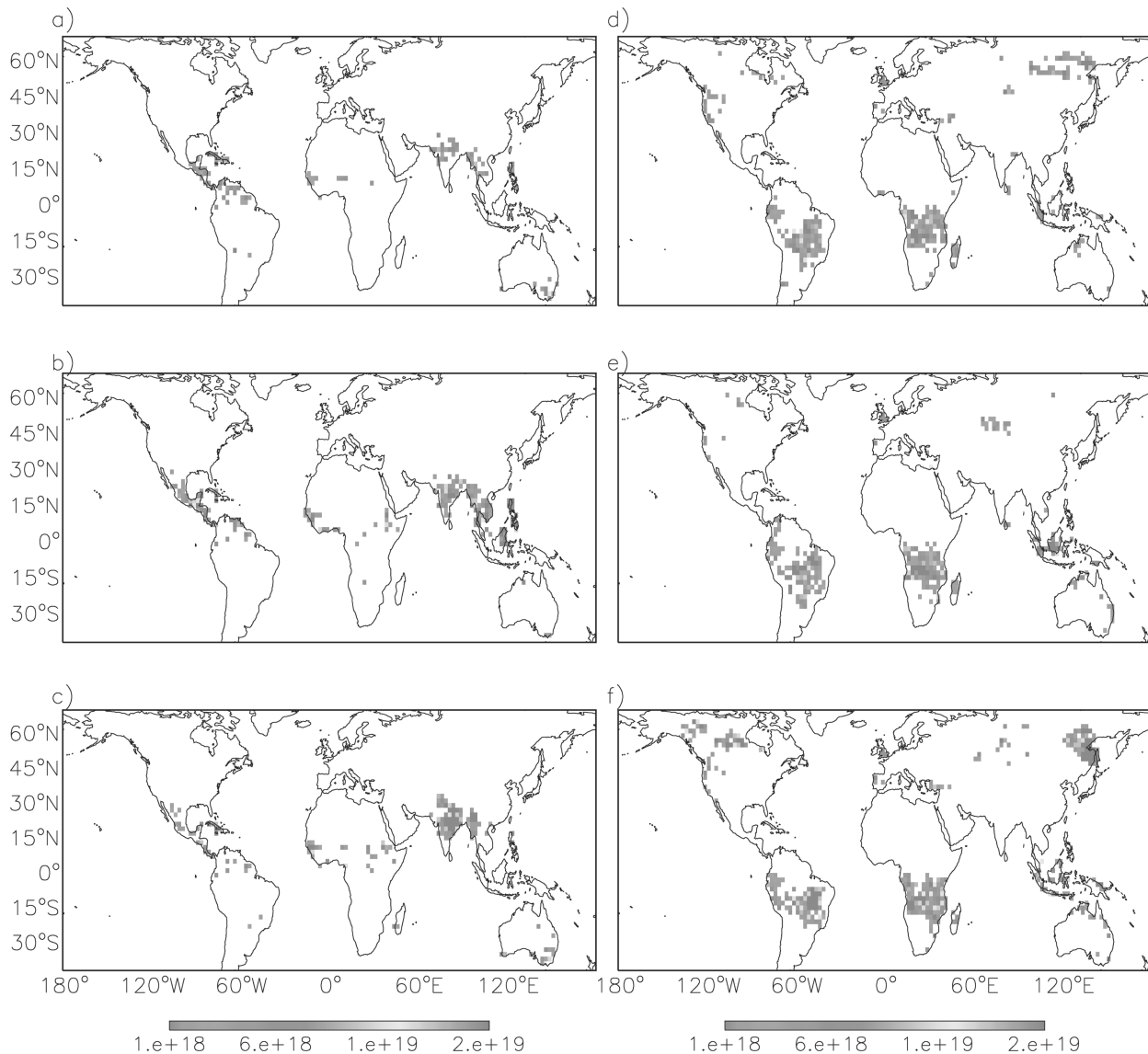
Figure 9. Interannual variation in biomass burning emissions (molecules CO cm^{-2} month^{-1}) for April a) 1997, b) 1998, and c) 1999, and August d) 1996, e) 1997, and f) 1998. See color version of this figure at back of this issue.

annual emissions of CO from biomass burning (437 Tg), about 210 Tg originates in the Northern Hemisphere south of 30°N and about 188 Tg comes from the Southern Hemisphere (Table 2); about 39 Tg are emitted annually north of 30°N.

[39] For Brazil, fires are concentrated along the southern edge of the Amazon rain forest and in the savannas that lie south and east of the rain forest (Figure 1). The monthly emissions maps derived from fire-count data show that burning begins in July and peaks generally in August and September (Figure 5b). While the majority of burning dwindles by October and November, a concentrated area of burning near the mouth of the Amazon River intensifies and continues through December (Figure 6).

[40] Fires in Africa south of the equator begin as early as May in Angola and Zaire in the western part of this region (Figure 6). Burning becomes more widespread by July from Angola east to Tanzania and Mozambique and down to the east coast of South Africa. By September and October, burning is concentrated in eastern Africa including Madagascar (Figure 6). The burning season for southern Africa generally ends before December (Figure 5b). *Cooke et al.* [1996] and *Justice et al.* [1996] found similar results by analyzing AVHRR fire-counts.

[41] The Indonesia and Malaysia region is characterized by infrequent large burning events that coincide with major ENSO-induced droughts [*Ropelewski and Halpert*, 1987; *Allan*, 1991; *Mori*, 2000]. These burning events generally occur during the Southern Hemisphere dry season, but have also occurred in February through May (Figure 5b). The concept of a mean seasonal variation is less appropriate for this region.

[42] The primary area of burning in Africa north of the equator lies in the savanna ecosystems between the Sahara

desert and central African rain forests (Figure 1). Burning usually occurs in the winter dry season, and begins in the Sahel by October (Figure 6). Fires spread south through November with highest fire-counts and emissions of CO evident between December and February (Figures 5c and 6). This pattern derived from satellite data is consistent with that described by *Menaut et al.* [1991] based on the ecology literature for western Africa. *Cooke et al.* [1996] found similar timing of burning by analyzing AVHRR fire-counts.

[43]   The Southeast Asia region is defined here as Myanmar, Thailand, Cambodia, Laos and Vietnam. Biomass burning is intense in this region, emitting large amounts of trace gases to the atmosphere (Figure 4) [*Elvidge and Baugh*, 1996]. The biomass burning season lasts from January to May, peaking in March (Figures 5c and 6). During this time, regional pollution episodes associated with biomass burning have been observed in nearby Hong Kong [*Liu et al.*, 1999; *Chan et al.*, 2000].

4.2.   Interannual Variability by Region

[44]   In this section we discuss interannual variability of biomass burning by region as inferred from TOMS AI data and we compare our results to other sources of information on the time dependence of biomass burning. ATSR fire-counts are the only data common to all regions with which we can evaluate interannual variability. Figures 8c–8h compare the $MRAI_{m,n}$ and Monthly Regional Fire-counts (MRF) from ATSR for six regions. (For each region, the largest peak in the $MRAI_{m,n}$ was used to normalize the MRF for the entire time period of fire-counts.) The seasonal variation of burning and relative year-to-year intensity derived from the TOMS AI is similar to those derived from ATSR data for Southeast Asia, Central America and Mexico, Brazil, Indonesia and Malaysia. This is not the case, however, for northern Africa and southern Africa (Figures 8g–8h) as discussed in sections 4.2.5 and 4.2.6.

4.2.1.   Indonesia and Malaysia

[45]   The TOMS AI shows that peak burning years for the Indonesia and Malaysia region are 1982–1983, 1991, and 1997–1998 (Figure 8c). These burning events coincided with major ENSO-induced droughts [*Ropelewski and Halpert*, 1987; *Allan*, 1991; *Mori*, 2000]. The ENSO event of 1997–1998 was the most extreme of the century, while the event of 1982–1983 was the second largest [*Wolter and Timlin*, 1998; *Glantz*, 2001].

[46]   The drought of 1982–1983 resulted in enormous forest fires, especially on the island of Borneo in East Kalimantan and the Malaysian state of Sabah [*Malingreau*, 1987]. These fires were estimated to cover about 5 million ha in Borneo [*Goldammer and Seibert*, 1990]. AI data clearly indicate large fires in New Guinea in October and November 1982, fires in Borneo and Sumatra in September and October 1982, and fires in Borneo again in March and April 1983.

[47]   The weaker, prolonged ENSO event of 1990–1995 resulted in drought and fires in 1991 and 1994 [*Allan and D'Arrigo*, 1999]. Large fires were observed in September and October 1991 on Sumatra and Borneo [*Brauer and Hisham-Hashim*, 1998]. *Fujiwara et al.* [1999] report that widespread forest fires occurred in Sumatra and southern Borneo from August to October 1994, a period lacking AI data. Based on reports in the literature and knowledge of ENSO-induced droughts, the TOMS AI data gap was filled

with a high burning year for 1994 similar in intensity to 1991, and with low burning years for 1995 and 1996.

[48]   The last major catastrophic fire event took place from August 1997 to April 1998 (Figure 8c) during a period of extreme drought. The ATSR World Fire Atlas indicates that fires in 1997 were widespread, occurring on many of Indonesian and Malaysian islands (i.e., southern Sumatra, southern Borneo, southern New Guinea, Sulawesi, and Java, as shown in Figure 2, August through November 1997). Concentrated fire-counts are seen on Sumatra, Borneo, and New Guinea (Figure 1a). However, fires in 1998 from January to May occurred predominately on Borneo in East Kalimantan, and the Malaysian state of Sabah (Figure 2). In East Kalimantan, approximately the same area that burned in the 1982–1983 fires burned again in the 1998 fires [*Mori*, 2000].

[49]   In high intensity burning events, such as forest fires in Indonesia and Malaysia, emissions of trace gases can be lofted out of the boundary layer and into the free troposphere because of convection generated by the fires. Traditionally, chemical tracer models emit trace gases from biomass burning directly into the first model layer or into the boundary layer. For these regions, it may be more appropriate to distribute these emissions over a larger vertical extent.

4.2.2.   South America

[50]   Figure 1 shows two major regions of biomass burning in South America. The first region of burning is predominately composed of Brazil, but also includes parts of Bolivia, Paraguay, and northern Argentina (Figure 3). There is significant interannual variability in $MRAI_{m,n}$ and there appears to be no systematic trend (Figure 8d). The interannual variability estimated by our method agrees well with the AI reported by *Gleason et al.* [1998] over Cuiaba, Brazil. Interannual variability is due likely to both year-to-year variation in climate and political incentives to clear land [*Sawyer*, 1990; *Kengen and Graca*, 1999]. *Gleason et al.* [1998] found that interannual variability depends primarily on the amount of rainfall received during the months when burning typically occurs, with most burning in the driest years. The AI signal is generally strongest over the continent (e.g., Figure 2 for August). The aerosol is transported off the coast over the Atlantic Ocean near Buenos Aires and São Paulo or over the Andes mountains near Ecuador [*Hsu et al.*, 1996]. The Brazil region is crossed by mountain ranges where orographic lifting is likely a mechanism for vertical transport of aerosol. The seasonal variation of biomass burning aerosol based on the work described here has been implemented in the GOCART (Georgia Tech/Goddard Global Ozone Chemistry Aerosol Radiation and Transport) model and the resulting aerosol optical depth compares well with AERONET observational data in Brazil [*Chin et al.*, 2002].

[51]   Biomass burning in the north of South America is concentrated largely in Colombia and Venezuela (Figure 1) and occurs from December to May (Figure 5c). ATSR fire-counts for 1996–2000 show substantial interannual variability (Figure 10a). Unfortunately, AI data cannot be used as a surrogate for variability in burning in this region. The AI signal is contaminated with aerosol from biomass burning in northern Africa. In January 1998, for example, a tongue of aerosol is seen to stretch westward from the African con-
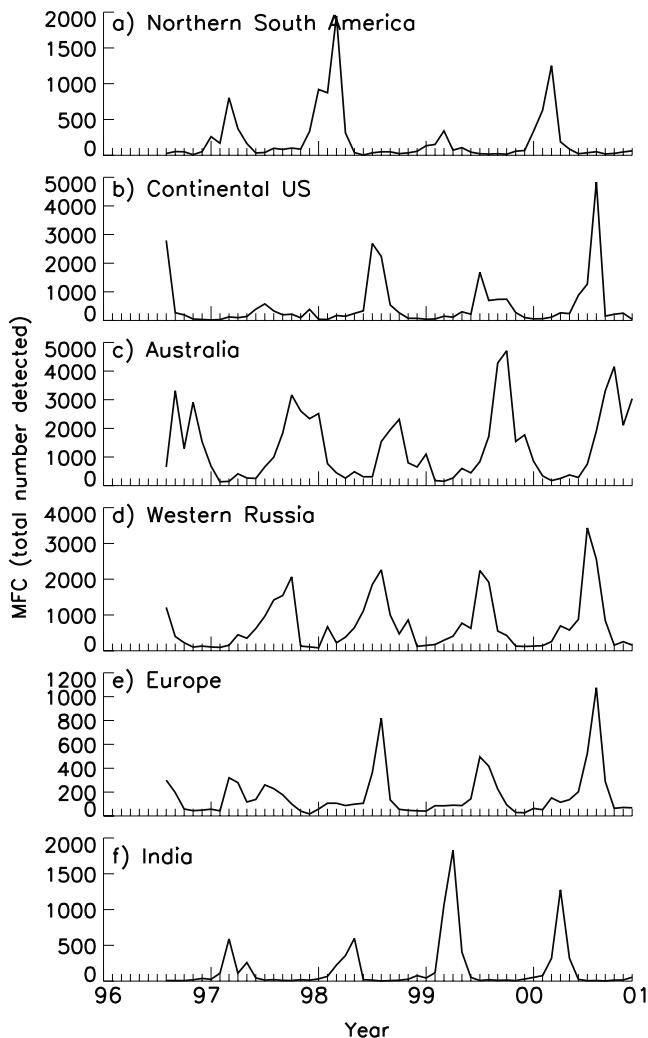
Figure 10. Total monthly ATSR fire-counts for a) northern South America, b) the Continental United States, c) Australia, d), Western Russia e) Europe, and f) India from August 1996 to December 2000.

tinent toward northern South America, though not quite reaching it this year (Figure 2). Desert dust from the Sahara is evident in the AI data for this region between May and August. *Herman et al.* [1997] report desert dust from Saharan dust storms reaching the Caribbean, and even into the Gulf of Mexico. As a result of these features, correlation between ATSR fire-counts and biomass burning aerosol is weak for northern South America (not shown). We chose not to use the $MRAI_{m,n}$ to estimate interannual variability of biomass burning. Instead emissions repeat from year to year prior to 1997. This should not introduce large errors in the annual emissions, as the amount of biomass burned in this region is small compared to the total for the northern tropics (Table 2).

4.2.3. Central America and Mexico

[52] The rates for deforestation for this region are estimated to have increased from 0.5% per year for the 1980s to 1.2% per year for 1990–1995 [*FAO*, 1995, 1997]. This trend is not readily apparent however in $MRAI_{m,n}$ (Figure 8e). Biomass burning aerosol from this region is readily

seen off the southern coast of Mexico over the Pacific Ocean and, to a lesser extent, off the northern coast of Mexico over the Bay of Campeche and the Gulf of Mexico (Figure 2 for May 1998 [*Rogers and Bowman*, 2001]). We limit our analysis to February through May because desert dust transported from the Sahara is evident during the summer months for this region (Figure 8e). An ENSO-induced drought resulted in a catastrophic burning event in the tropical forests of southern Mexico and Central America from April to June 1998, with the most intense smoke from mid-May through late May (Figure 2 for May, Figure 8e, and Figure 9b [*Peppler et al.*, 2000; *Cheng and Lin*, 2001]).

4.2.4. Southeast Asia

[53] Considerable interannual variation is evident from the AI data as shown in Figure 8f. This is supported by the ATSR fire-counts (Figures 9a–9c). While the ATSR signal is strong within the region, the corresponding signal in AI data is seen primarily downwind, over the lowlands of southern China and Gulf of Tonkin (Figure 2 for March 1998). Prevailing winds transport the aerosol northeast from the source region at this time of year [*Bey et al.*, 2001].

4.2.5. Northern Africa

[54] Contamination of the AI signal from biomass burning with desert dust from the Sahara is a problem for this region (Figure 8g), even though the biomass burning season is out of phase with the peak season for desert dust. Contribution of desert dust to AI reaches a maximum in summer, covering most of the Middle East, northern Africa, and the tropical Atlantic Ocean as far west as the Caribbean Sea (Figure 2). There are desert dust signals observed in northern Africa at all times of the year, especially over a dry lake bed in the Sahel near Lake Chad [*Herman et al.*, 1997; *Ginoux et al.*, 2001]. As a result, the AI during the biomass burning season is likely to be contaminated with a minor component from desert dust aerosol.

[55] The AI signal from biomass burning in northern Africa is strongest over land near the west coast, especially from Senegal south to Gabon on the equator, and over the Gulf of Guinea (see December 1997 to March 1998 in Figure 2). The AI signal is not strong over much of the fire region, especially in east Africa. Savanna fires are not generally energetic enough to produce convection, except possibly in the humid Guinean and southern Sudanese zones where the total biomass load is high [*Delmas et al.*, 1991; *Menaut et al.*, 1991]. Emissions are likely trapped below the trade wind inversion in the tropics (∼3–5 km) and disperse in the boundary layer [*Andreae*, 1991], especially in the dry Sahelian zone where fuel loads are low [*Delmas et al.*, 1991; *Menaut et al.*, 1991]. TOMS sensitivity decreases toward the surface. Aerosol in western Africa are generally transported over the ocean by prevailing trade winds and are lofted near the coast by oceanic air masses moving to the north from the Gulf of Guinea [*Marenco et al.*, 1990].

[56] Our analysis of the $MRAI_{m,n}$ is limited to October through March for northern Africa, since widespread burning usually ends by April (Figure 8g). The $MRAI_{m,n}$ for northern Africa does not mimic the year-to-year changes seen in ATSR fire-counts, perhaps because of contamination of the AI by desert dust. Both data sets suggest much less

interannual variation in fire activity than in other regions, and this is likely because most fires in Africa are in the savannas, which have relatively low fuel loads compared to forests and high burn frequency [e.g., *Delmas et al.*, 1991; *Menaut et al.*, 1991]. We adopted the same emissions each year for northern Africa, given the lack of reliable information on yearly variations for the entire period.

[57] Using AVHRR data, *Cooke et al.* [1996] showed that the timing and number of fires for specific regions in Africa varied substantially from year to year for 1984 to 1989. However, they provide results only for selected $5° \times 5°$ grid boxes, making it difficult to compare their results to those from AI data. *Barbosa et al.* [1999], also using AVHRR fire-counts, estimated that the biomass burned in 1987–1988 was half that in 1989–1990. They attribute this difference to an ENSO-induced drought in southern Africa in 1986–1987 that decreased the amount of biomass available for burning in 1987–1988. For years other than 1987–1988, the estimated amount of biomass burned was within ~15% of the mean for 1985–1991. The results of Barbosa et al. suggest that our assumption of no interannual variability in African emissions may be reasonable except in years affected by extreme drought.

4.2.6. Southern Africa

[58] For this region the AI signal is generally strongest over the ocean and near the west coast of Africa from Gabon south to northern Namibia (Figure 2 for August). TOMS more easily detects the aerosol after it is transported by prevailing easterlies from the highland plateau over low-lying coastal plains and the Atlantic Ocean. A minor component of total aerosol is observed to leave the continent from the southeastern coast of South Africa as well.

[59] The $MRAI_{m,n}$ does not compare well enough with ATSR fire-counts to estimate interannual variation of biomass burning emissions for southern Africa (Figure 8h). A smaller peak associated with the transport of biomass burning aerosol from northern Africa is seen in Figure 8h centered around January. While $MRAI_{m,n}$ appears to predict the onset and magnitude of the early part of the burning season, it does not predict burning in the later part of the season, especially fires in eastern Africa and Madagascar. Consequently, we use the mean seasonal variation in biomass burning for this region, except for 1996–2000 where we use ATSR fire-count data to estimate interannual variation as discussed in section 3.3. The mean seasonal variation of biomass burning aerosol optical depth as simulated by the GOCART model compares well with AERONET observational data in southern Africa for 1995 to 1998 [*Chin et al.*, 2002].

4.2.7. Boreal Forests of Asiatic Russia and North America

[60] We evaluated $MRAI_{m,n}$ using statistics for the total area-burned (TAB) for boreal forests in Canada, Alaska and Russia. Boreal forest fires generally take place from May to September when temperatures are higher and lightning strikes occur more frequently [*Skinner et al.*, 2000]. Lightning causes about a third of fires in boreal forests of North America, but account for over three quarters of total area burned [*Stocks*, 1991; *Weber and Stocks*, 1998]. In Canada most fires are minor, but the 2–3 % of fires larger than 200 ha account for 98% of total area burned each year. Figure 8a shows TAB in North Amer-

ican boreal forests from 1979 to 1998 based on official government statistics from Canada and Alaska [*Johnston*, 2001, available at http://www.nrcan-rncan.gc.ca/cfs-scf/science/prodserv/firereport/firereport_e. html; *Alaska Division of Forestry* (*ADF*), 2001, available at http://www.dnr.state.ak.us/forestry/firestats.htm]. For the period, an average of 2.9 million ha burned annually, but there is significant year-to-year variability.

[61] Over two-thirds of the world's boreal forests lie in Russia. Most fires are thought to be caused by lightning, because of the remoteness of the forests [*Stocks*, 1991]. Most fires are likely stand-replacement crown fires as opposed to ground fires, contrary to reports in the Russian literature [*Kasischke et al.*, 1999]. Unfortunately, the Russian TAB statistics are of questionable quality and account only for areas where active fire suppression occurred [*Kasischke et al.*, 1999]. As a result, official statistics likely underestimate the TAB in all of Asiatic Russia. In 1987, TAB was reported to be 1.3 million ha (Figure 8b), but independent estimates using analysis of satellite imagery were about 12 million ha for eastern Russia [*Kasischke et al.*, 1999].

[62] $MRAI_{m,n}$ for Canada and Alaska and Asiatic Russia are shown in Figures 8a and 8b, respectively. Detection of forest fire aerosol by TOMS over Canada and Greenland during this period is also discussed by *Hsu et al.* [1999a]. Stars in the figure correspond to integrated total area (ITA) under the $MRAI_{m,n}$ curve for a year's summer season. The general shape and intensity of ITA is similar to the TAB time series (Figure 8a). One notable deviation occurs in 1988, attributable to contamination of the region with aerosol transported northward from the contiguous U. S. Major forest fires occurred in the U.S. in the very dry summer of 1988, for example, the Yellowstone National Park fires. Minor contamination of the region occurred also in 1984 and 1987 from fires in eastern Russia near the Sea of Okhotsk.

[63] We assume that the $MRAI_{m,n}$ is a reasonable surrogate for TAB in Russia based on the results of Figure 8a for North America. The ITA indicates that enhanced fire activity occurred in the mid-1980s, 1996, and 1998 (Figure 8b). The TAB for Russia actually appears to agree with the ITA beginning after 1988 possibly indicating the quality of the TAB statistics is improving for Russia. For the period for which there are fire-count data, the greatest concentration of fires occurred in the far east of Russia along the Sea of Okhotsk in the summers of 1996 and 1998 (Figures 9d and 9f).

4.2.8. Other Regions

[64] Other regions with fire-counts (Figure 1) include the continental U.S., Australia, Western Russia, Europe, and India. For these regions, $MRAI_{m,n}$ was not calculated for the reasons discussed below.

4.2.8.1. Continental United States

[65] Biomass burning in the continental U.S. is associated primarily with forest wild fires and controlled burning generally from June to September (Figure 10b). Annual CO emissions are quite small compared to that for boreal forests in Canada and Alaska (Figure 4). On average, less than 5 Tg CO is emitted annually from the continental U.S. High signals in AI only appear for the summers of 1987 in the Pacific Northwest, and 1988 and 1990 in the western U.S. In general, most of the large fires occur in the

western U.S. where the AI signal is often influenced by desert dust.

4.2.8.2. Australia

[66] Most fires occur in the north and east of Australia (Figure 1). The burning season usually begins in August in the northern parts of Northern Territory and Queensland and ends by November (Figure 10c). In the eastern part of Australia, especially southeastern Queensland, burning generally begins in September and ends by December (Figure 6).

[67] Desert dust contamination is a problem for this region, especially near Lake Eyre (e.g., Figure 2, November). Unfortunately, drought conditions in Australia lead to stronger than normal dust events. These make it impossible to extract a component of aerosol from biomass burning. We estimate interannual variation for the years with ATSR data as discussed in section 3.3. Rainfall in Australia is strongly connected to ENSO events, as it is for Indonesia to the north [*Ropelewski and Halpert*, 1987; *Allan*, 1991]. Burning in Western Australia from November 1997 to January 1998 was probably related to the ENSO-induced drought of 1997–1998, as significant fire-counts are not seen there in the other years with data. The signal in the fire-counts from Western Australia during this time is not easily seen in Figure 10c which includes all fire-counts in Australia.

4.2.8.3. Western Russia and Europe

[68] Burning in western Russia and Europe generally occurs from spring to fall and is associated with agricultural residues burned in the fields (Figures 10d–10e). There are few areas of concentrated fire-counts (Figure 1a) and the AI signal is weak. In these regions, aerosol from industrial sources, such as sulfate, black carbon, and organic carbon, dominate the total aerosol load [*Chin et al.*, 2002]. As a result, we do not calculate $MRAI_{m,n}$ for this region. One area of concentrated fire-counts is in northwestern Spain (Figure 1a). Seasonal burning of agricultural residues in the fields associated with corn production occurs in northwestern Spain [*U.S. Department of Agriculture*, 1994]. ATSR fire-counts indicate burning occurs in spring before planting. The largest burning during the period of ATSR data, however, occurred in August 1998 before the typical harvest time. There is not a strong AI signal associated with this burning.

4.2.9. India

[69] While fire-counts are detected over all of India, the most intense region of burning is in the northeast, especially the state of Orissa southwest of Calcutta [*Elvidge and Baugh*, 1996] during March, April, and May. ATSR fire-counts indicate that the 1999 burning season was very intense as compared to the two previous seasons (Figures 9a–9c and 10f). Fires in 1999 featured an intense area of burning along the foothills of the Himalayas in the Ganges River valley not seen in either 1997 or 1998. We do not derive $MRAI_{m,n}$ for India because aerosols from other sources contribute significantly to the AI signal, such as desert dust from northwestern India and Pakistan, and aerosols from fossil fuel and biofuel combustion [*Rasch et al.*, 2001; *Chin et al.*, 2002].

5. Trends in Biomass Burning Emissions of CO

[70] We applied our interannual and seasonal scaling factors to estimate emissions of CO from biomass burn-
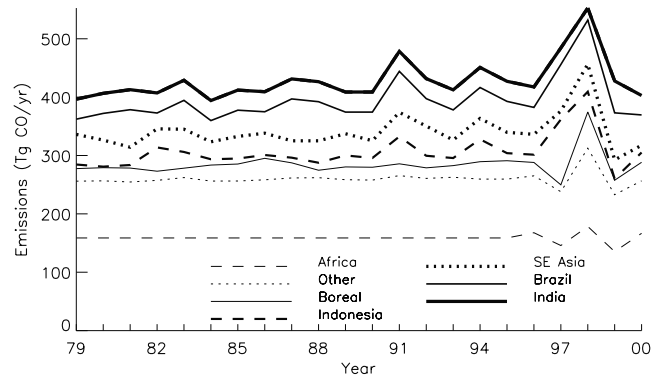

Figure 11. Time series of annual emission rates (Tg CO yr^{-1}) by region for 1979–2000. The contribution of each region is "stacked" on the contribution of each region plotted below it, so that the line for India represents the total global emission rate. The annual emissions attributed to "other" regions include northern South America, Australia, the Continental U.S., Europe, etc.

ing. Figure 11 shows the regional contribution to the global annual emission rate of CO for 1979–2000, while Figure 12 shows the emissions by season. Note that Figure 11 shows the cumulative emissions by region, while Figure 12 does not. Africa is the largest contributor to the annual emission rate, with the "other" region being the second largest. The latter region is largely composed of those regions discussed in section 4.2.8 for which interannual variability could not be computed from TOMS AI data (i.e., northern South America, Australia, Continental U.S., and Europe) and Central America and Mexico. Overall, none of these regions dominate the total annual emissions for this region shown in Figure 11. Generally, northern South America, Central America, and Mexico contribute the most to the "other" emissions from March to May (Figure 5), Europe and the Continental U.S. dominate from June to August (Figures 10b and 10f), and Australia dominates from September to November (Figure 10c).

[71] No trend in biomass burning emissions of CO is apparent in any region or the globe over the last two decades on either an annual or a seasonal basis, but there is significant interannual variability in Indonesia and Malaysia, Brazil, Canada and Alaska, and Asiatic Russia (Figures 11 and 12). The lack of trends may result in part from the lack of significant change in the average rate of deforestation between 1980 and 1995 for most regions of the developing world [*FAO*, 1993, 1995, 1997]. There is an apparent upward trend in emissions from Indonesia and Malaysia over the two decades, but this is caused by the large burning event in 1997–1998 associated with the ENSO-induced drought (section 4.2.1). Future such droughts are likely to result in catastrophic fires due to pressure from the region's growing population. Most fires during the 1997–1998 event were intentionally set as a method to clear land for farming [*Brauer and Hisham-Hashim*, 1998].

[72] The season with the largest interannual variability is September to November (Figure 12d); this period corresponds to the Southern Hemisphere burning season with the
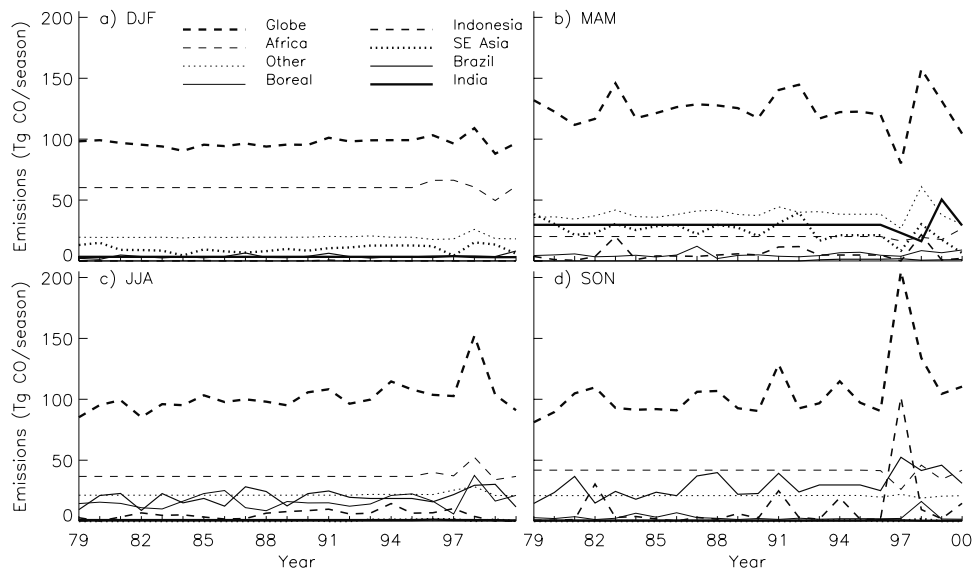
Figure 12. Time series of seasonal emission rates (Tg CO/season) for 1979–2000 for a) December to February, b) March to May, c) June to August, and d) September to November. The seasonal emissions attributed to "other" regions include northern South America, Australia, the Continental U.S., Europe, etc.

Indonesia and Malaysia, and the Brazilian regions contributing to the interannual variability. There is also high interannual variability in March to May, due to emissions from Southeast Asia and from the Indonesia and Malaysia regions (Figure 12b). There is least variability in December to February, perhaps because we do not prescribe any such variability in northern Africa prior to 1996. Northern Africa is the largest contributor to global CO emissions from December to February, while southern Africa is the largest contributor from June to August.

[73] A number of large biomass burning events occurred during the time period covered by TOMS AI data. The largest single burning event for all regions occurred in August to November 1997 and March to April 1998 in Indonesia and Malaysia (Figure 8c). For these periods, we estimate emissions of about 133 Tg CO for the region in 1997 and 36 Tg CO in 1998 (Table 5). *Levine* [1999] estimated that 38–114 Tg CO resulted from fires in Kalimantan and Sumatra in 1997 alone using area burned estimates from satellite imagery; note this does not include emissions from fires on other islands of the Indonesian archipelago. The uncertainty of both estimates depend on assumptions such as the total biomass consumed, types of biomass consumed, amount of smoldering and flaming combustion, and the CO emission factors. For the entire burning event in the Indonesia and Malaysia region in 1997 to 1998, we estimate about 170 Tg CO were released (i.e., about one-third of the global mean annual emissions of CO from biomass burning). In comparison, the 1982–1983 burning event released about 52 Tg CO (Table 5). Interestingly, emissions from fires in 1997 were reported to be largely from the burning of peat rather than forests [*Levine*, 1999; *Muraleedharan et al.*, 2000].

[74] Other significant fire events include forest fires in northern China and Siberia in May 1987, eastern Russia during the summer of 1998, and in Mexico and Central

America in May 1998 (Table 5). There are two differing estimates of the area burned in the spring of 1987 during the Great China fire. *Cahoon et al.* [1991] used AVHRR satellite data of burn scars to estimate that 1 million ha burned in China and 3.6 million ha burned in eastern Russia. In a later paper, again using AVHRR burn scars, *Cahoon et al.* [1994] estimated 14.5 million ha burned and estimated that about 36 Tg CO were emitted during the Great China Fire. From our MRAI$_{m,n}$-adjusted emission inventory for the same period, we derive emissions of about 20 Tg CO for the Asiatic Russia region that includes northern China. *Kasischke and Bruhwiler* [2002] using fire statistics and satellite imagery estimated that 17.9 million ha burned in the boreal forests of Russia and North America in 1998 releasing between 105 and 145 Tg CO; this included 20 Tg CO from peatland burning. About two-thirds of the emissions from this estimate were in Russia. From our MRAI$_{m,n}$-adjusted emission inventory for the same period, we also estimate about two-thirds of the total boreal forest emissions during 1998 were from

Table 5. Emissions of CO[a] From Large Biomass Burning Events

Location	Period	Total Emission, Tg CO yr^{-1}	Literature Estimates
Indonesia and Malaysia	1997	133	38–114[b]
	1997–1998	170	
	1982–1983	52	
Asiatic Russia/China	May–June 1987	20	36[c]
Mexico and C. America	April–June 1998	24	
Boreal Forests	Summer 1998	69	105–145[d]
Globe	Annual Mean	437	

[a]CO emission is expressed as Tg CO.
[b]*Levine* [1999].
[c]*Cahoon et al.* [1994].
[d]*Kasischke and Bruhwiler* [2002].

Asiatic Russia, 47 Tg out of a total of 69 Tg CO. We estimate emissions of about 21 Tg CO from fires in Canada and Alaska in that same year. Our estimate is lower largely because we assumed a lower average release of carbon (11,250 kg C/ha) than Kasischke et al. (9900–32,500 kg C/ha). Kasischke et al. argued that boreal forest fires are mostly high-intensity crown fires in both Russia and North America, which have a high release of carbon per ha burned. Our estimate for CO from fires in Mexico and Central America from April to June 1998 is 24 Tg.

6. Summary

[75] Using remote-sensed observations of fire-counts, we estimated the mean seasonal variation of biomass burning using 4 years of ATSR and 1–2 years of AVHRR fire-count data. The resulting product has monthly temporal resolution and $1° \times 1°$ spatial resolution. Maximum amounts of biomass burning occur in February to April in the Northern Hemisphere dry season and in August to October in the Southern Hemisphere dry season. There are minimum amounts of biomass burning in May and June, and in November, although burning can occur at any time of year. The major burning regions are Southeast Asia, Africa north of the equator, Brazil, Indonesia and Malaysia, and Africa south of the equator.

[76] We estimated interannual variation of biomass burning based on TOMS AI data for 1979 to 2000. This product was used to adjust an annual mean emission inventory, in order to capture interannual variability in biomass burning. We processed the TOMS AI data into a Monthly Regional Aerosol Index ($MRAI_{m,n}$) and compared it to ATSR fire-count data and to area burned estimates reported in the literature. The interannual variation was constructed for Canada and Alaska, Central America and Mexico, Brazil, Asiatic Russia, Indonesia and Malaysia, and Southeast Asia. For the remaining world regions, we use the mean seasonal variation because of the sparseness of fires, and/or the mixing of biomass burning aerosol with desert dust and aerosol associated with fossil fuel and biofuel combustion. Interannual variation of burning for Africa estimated by the TOMS AI did not compare well to fire-count observations. Fire-counts suggest there is little interannual variation in total biomass burning from northern and southern Africa, at least for 1996 to 2000. Barbosa et al. [1999] found small interannual variations for 1985 to 1991, except for one year when burning was very low because of a drought the previous year that had reduced the fuel load. TOMS AI data could not be used to spatially resolve interannual variation of emissions beyond the regional scale. However, for August 1996 through July 2000, emissions were resolved with higher spatial resolution by using fire-count data from ATSR.

[77] We applied our interannual and seasonal scaling factors to estimate emissions of CO from biomass burning. We found that there were no annual or seasonal trends in biomass burning emissions of CO over the last two decades globally or for any region, but there was significant interannual variability, especially for Indonesia and Malaysia, Brazil, Southeast Asia, and the boreal regions. For instance, the global CO emissions from biomass burning in 1997, 511 Tg, and 1998, 565 Tg, were significantly higher than in 1999, 429 Tg. The largest releases of CO resulted from uncontrolled forest wildfires during the last two decades and were often associated with ENSO-induced droughts. Several catastrophic fires occurred in 1997 and 1998 during the most extreme ENSO event of the century. Widespread wildfires occurred in Indonesia and Malaysia from August to October 1997 and March and April 1998. About 170 Tg CO were released, which is three times greater than the large burning event in 1982 and 1983 in the same region and over one-third of the annual mean global emissions. We estimate that about 70 Tg CO were released from widespread wildfires in the boreal regions in the summer of 1998, and 24 Tg CO in April and May 1998 in Central America and Mexico. Another notable wildfire occurred in May 1987 in Asiatic Russia and northern China, 20 Tg CO.

[78] The time-dependent emissions inventory for biomass burning created using the methods presented here has been used in 3-d model studies of the emissions of aerosols from biomass burning [Chin et al., 2002], pollution transport from Asia [Staudt et al., 2001], ozone over Oceania [Chandra et al., 2002], ozone in the tropics [Martin et al., 2002a], and a retrieval of NO_2 from GOME [Martin et al., 2002b]. The time-dependent emission inventory is currently being used in a study of the interannual variability of CO (Duncan et al., in preparation; Duncan and Logan, in preparation).

References

Alaska Division of Forestry (ADF), Fire Statistics for the State of Alaska, 2001.

Allan, R. J., Australasia, in Teleconnections Linking Worldwide Climate Anomalies, edited by M. H. Glantz, R. W. Katz, and N. Nicholls, pp. 73–120, Cambridge Univ. Press, New York, 1991.

Allan, R. J., and R. D. D'Arrigo, Persistent ENSO sequences: How unusual was the 1990–1995 El Niño?, Holocene, 9(1), 101–118, 1999.

Andreae, M. O., Biomass burning: Its history, use, and distribution and its impact on environmental quality and global climate, in Global Biomass Burning: Atmospheric, Climatic, and Biospheric Implications, edited by J. S. Levine, pp. 3–21, MIT Press, Cambridge, Mass., 1991.

Andreae, M. O., and P. Merlet, Emission of trace gases and aerosols from biomass burning, Global Biogeochem. Cycles, 15, 955–966, 2001.

Andreae, M. O., E. Atlas, H. Cachier, W. R. Cofer III, G. W. Harris, G. Helas, R. Koppmann, J.-P. Lacaux, and D. E. Ward, Trace gas and aerosol emissions from savanna fires, in Biomass Burning and Global Change, edited by J. S. Levine, pp. 278–295, MIT Press, Cambridge, Mass., 1996.

Arino, O., and J.-M. Melinotte, Fire index atlas, Earth Obs. Q., 50, 11–16, 1995.

Arino, O., and S. Plummer (Eds.), Along Track Scanning Radiometer World Fire Atlas: Validation of the 1997–98 Active Fire Product, ESA-ESRIN, Italy, 2001.

Arino, O., J.-M. and Rosaz, 1997 and 1998 World ATSR Fire Atlas using ERS-2 ATSR-2 data, in Proceedings of the Joint Fire Science Confer-

ence, Boise, Idaho, pp. 177–182, University of Idaho and the International Association of Wildland Fire, 1999.

Barbosa, P. M., J.-M. Grégoire, and J. M. C. Pereira, An algorithm for extracting burned areas from time series of AVHRR GAC data applied at a continental scale, *Remote Sens. Environ.*, 69, 253–263, 1999.

Bey, I., D. J. Jacob, R. M. Yantosca, J. A. Logan, B. Field, A. M. Fiore, Q. Li, H. Liu, L. J. Mickley, and M. Schultz, Global modeling of tropospheric chemistry with assimilated meteorology: Model description and evaluation, *J. Geophys. Res.*, 106, 23,073–23,096, 2001.

Brauer, and Hisham-Hashim, Fires in Indonesia: Crises and reaction, *Environ. Sci. Technol.*, 32, A404–A407, Sept. 1 1998.

Browell, E. V., et al., Ozone and aerosol distributions and air mass characteristics over the South Atlantic Basin during the burning season, *J. Geophys. Res.*, 101, 24,043–24,068, 1996.

Cahoon, D. R., Jr., et al., The great Chinese fire of 1987, a view from space, in *Global Biomass Burning: Atmospheric, Climatic, and Biospheric Implications*, edited by J. S. Levine, pp. 61–67, MIT Press, Cambridge, Mass., 1991.

Cahoon, D. R., Jr., B. J. Stocks, J. S. Levine, W. R. Cofer III, and J. M. Pierson, Satellite analysis of the severe 1987 forest fires in northern China and southeastern Siberia, *J. Geophys. Res.*, 99, 18,627–18,638, 1994.

Chan, L. Y., C. Y. Chan, H. Y. Liu, S. Christopher, S. J. Oltmans, and J. M. Harris, A case study on the biomass burning in Southeast Asia and enhancement of tropospheric ozone over Hong Kong, *Geophys. Res. Lett.*, 27, 1479–1482, May 15 2000.

Chandra, S., J. R. Ziemke, P. K. Bhartia, and R. V. Martin, Tropical tropospheric ozone: Implications for biomass burning, *J. Geophys. Res.*, 107(D14), 4188, doi:10.1029/2001JD000447, 2002.

Cheng, M.-D., and C.-J. Lin, Receptor modeling for smoke of 1998 biomass burning in Central America, *J. Geophys. Res.*, 106, 22,871–22,886, 2001.

Chiapello, I., J. M. Prospero, J. R. Herman, and N. C. Hsu, Detection of mineral dust over the North Atlantic Ocean and Africa with the Nimbus 7 TOMS, *J. Geophys. Res.*, 104, 9277–9291, 1999.

Chiapello, I., P. Goloub, D. Tanre, A. Marchand, J. Herman, and O. Torres, Aerosol detection by TOMS and POLDER over oceanic regions, *J. Geophys. Res.*, 105, 7133–7142, 2000.

Chin, M., P. Ginoux, S. Kinne, O. Torres, B. Holben, B. Duncan, R. Martin, J. Logan, A. Higurashi, and T. Nakajima, Tropospheric aerosol optical thickness from the GOCART model and comparisons with satellite and sunphotometer measurements, *J. Atmos. Sci.*, 59, 461–483, 2002.

Cofer, W. R., III, E. L. Winstead, B. J. Stocks, L. W. Overbay, J. G. Goldammer, D. R. Cahoon, and J. S. Levine, Emissions from boreal forest fires: Are the atmospheric impacts underestimated?, in *Biomass Burning and Global Change*, edited by J. S. Levine, pp. 834–839, MIT Press, Cambridge, Mass., 1996a.

Cofer, W. R., III, J. S. Levine, E. L. Winstead, D. R. Cahoon, D. I. Sebacher, J. P. Pinto, and B. J. Stocks, Source compositions of trace gases released during African savanna fires, *J. Geophys. Res.*, 101, 23,597–23,602, 1996b.

Cofer, W. R., III, E. L. Winstead, B. J. Stocks, J. G. Goldammer, and D. R. Cahoon, Crown fire emissions of CO_2, CO, H_2, CH_4, and TNMHC from a dense jack pine boreal forest fire, *Geophys. Res. Lett.*, 25, 3919–3922, 1998.

Cooke, W. F., B. Koffi, and J. M. Gregoire, Seasonality of vegetation fires in Africa from remote sensing data and application to a global chemistry model, *J. Geophys. Res.*, 101, 21,051–21,065, 1996.

Crutzen, P. J., and M. O. Andreae, Biomass burning in the tropics: Impact on atmospheric chemistry and biogeochemical cycles, *Science*, 250, 1669–1678, 1990.

Dave, J. V., Effect of aerosols on the estimation of total ozone in an atmospheric column from the measurement of its ultraviolet radiance, *J. Atmos. Sci.*, 35, 899–911, 1978.

Delmas, R., J.-P. Lacaux, J. C. Menaut, L. Abbadie, X. Le Roux, G. Helas, and J. Lobert, Nitrogen compound emission from biomass burning in tropical African savanna FOS/DECAFE 1991 Experiment (Lamto, Ivory Coast), *J. Atmos. Chem.*, 22, 175–193, 1995.

Delmas, R. A., P. Loudjani, A. Podaire, and J.-C. Menaut, Biomass burning in Africa: An assessment of annually burned biomass, in *Global Biomass Burning, Atmospheric, Climatic, and Biospheric Implications*, edited by J. S. Levine, pp. 126–132, MIT Press, Cambridge, Mass., 1991.

DeLuisi, J., E. Dutton, K. Coulson, T. Defoor, and B. Mendonca, On some Radiative features of the El Chichón volcanic stratospheric dust cloud and a cloud of unknown origin observed at Mauna Loa, *J. Geophys. Res.*, 88, 6769–6772, 1983.

Dozier, J., A method for satellite identification of surface temperature fields of subpixel resolution, *Remote Sens. Environ.*, 11, 221–229, 1981.

Dwyer, E., S. Pinnock, J.-M. Grégoire, and J. M. C. Pereira, Global spatial and temporal distribution of vegetation fire as determined from satellite observations, *Int. J. Remote Sens.*, 21, 1289–1302, 2000.

Elvidge, C. D., and K. E. Baugh, Survey of fires in Southeast Asia and India during 1987, in *Biomass Burning and Global Change*, edited by J. S. Levine, pp. 663–670, MIT Press, Cambridge, Mass., 1996.

Eva, H., and E. F. Lambin, Remote sensing of biomass burning in tropical regions: Sampling issues and multisensor approach, *Remote Sens. Environ.*, 64, 292–315, 1998.

FAO, Forest resources assessment 1990: Tropical countries, *FAO For. Pap. 112*, Food and Agric. Organ. of the United Nations, Rome, Italy, 1993.

FAO, Forest resources assessment 1990: Global synthesis, *FAO For. Pap. 124*, Food and Agric. Organ. of the United Nations, Rome, Italy, 1995.

FAO, State of the world's forest 1997, Food and Agric. Organ. of the United Nations, Rome, Italy, 1997.

Ferek, R. J., J. S. Reid, P. V. Hobbs, D. R. Blake, and C. Liousse, Emission factors of hydrocarbons, halocarbons, trace gases and particles from biomass burning in Brazil, *J. Geophys. Res.*, 103, 32,107–32,118, 1998.

Fiocco, G., M. Cacciani, A. G. di Sarra, D. Fua, P. Colagrande, G. De Benedetti, P. Di Girolamo, and R. Viola, The evolution of the Pinatubo stratospheric aerosol layer observed by lidar at South Pole, Rome, Thule: A summary of results, in *The Mount Pinatubo Eruption Effects on the Atmosphere and Climate*, NATO ASI Ser., vol. 42, edited by G. Fiocco, D. Fua, and G. Visconti, pp. 17–32, Springer-Verlag, New York, 1996.

Fromm, M., et al., Observations of boreal forest fire smoke in the stratosphere by POAM III, SAGE II, and Lidar in 1998, *Geophys. Res. Lett.*, 27, 1407–1410, 2000.

Fujiwara, M., K. Kita, S. Kawakami, T. Ogawa, N. Komala, S. Saraspriya, and A. Suripto, Tropospheric ozone enhancements during the Indonesian forest fire events in 1994 and 1997 as revealed by ground-based observations, *Geophys. Res. Lett.*, 26, 2417–2420, 1999.

Galanter, M., H. Levy II, and G. Carmichael, Impacts of biomass burning on tropospheric CO, NO_x, and O_3, *J. Geophys. Res.*, 105, 6633–6653, 2000.

Garstang, M., P. D. Tyson, R. Swap, M. Edwards, P. Kallberg, and J. A. Lindsay, Horizontal and vertical transport of air over southern Africa, *J. Geophys. Res.*, 101, 23,721–23,736, 1996.

Ginoux, P., M. Chin, I. Tegen, J. Prospero, B. Holben, O. Dubovik, and S.-J. Lin, Sources and global distributions of dust aerosols simulated with the GOCART model, *J. Geophys. Res.*, 106, 20,255–20,273, 2001.

Glantz, M. H., *Currents of Change, Impacts of El Niño and La Niña on Climate and Society*, pp 84–100, Cambridge Univ. Press, New York, 2001.

Gleason, J. F., N. C. Hsu, and O. Torres, Biomass burning smoke measured using backscattered ultraviolet radiation: SCAR-B and Brazilian smoke interannual variability, *J. Geophys. Res.*, 103, 31,969–31,978, 1998.

Goldammer, J. G., and B. Seibert, The impact of droughts and forest fires on tropical lowland rain forest of East Kalimantan, in *Fires in the Tropical Biota, Ecosystem Processes and Global Challenges*, edited by J. G. Goldammer, pp. 11–31, Springer-Verlag, New York, 1990.

Goloub, P., and O. Arino, Verification of the consistency of Polder Aerosol Index over land with ATSR-2/ERS-2 fire product, *Geophys. Res. Lett.*, 27, 899–902, 2000.

Hao, W. M., and M.-H. Liu, Spatial and temporal distribution of tropical biomass burning, *Global Biogeochem. Cycles*, 8, 495–503, 1994.

Hegg, D. A., L. F. Radke, P. V. Hobbs, R. A. Rasmussen, and P. J. Riggan, Emissions of some trace gases from biomass fires, *J. Geophys. Res.*, 95, 5669–5675, 1990.

Herman, J. R., P. K. Bhartia, O. Torres, C. Hsu, C. Seftor, and E. Celarier, Global distribution of UV-absorbing aerosols from Nimbus 7/TOMS data, *J. Geophys. Res.*, 102, 16,911–16,922, 1997.

Hsu, N. C., J. R. Herman, P. K. Bhartia, C. J. Seftor, O. Torres, A. M. Thompson, J. F. Gleason, T. F. Eck, and B. N. Holben, Detection of biomass burning smoke from TOMS measurements, *Geophys. Res. Lett.*, 23, 745–748, 1996.

Hsu, N. C., J. R. Herman, J. F. Gleason, O. Torres, and C. J. Seftor, Satellite detection of smoke aerosols over a snow/ice surface by TOMS, *Geophys. Res. Lett.*, 26, 1165–1168, 1999a.

Hsu, N. C., J. R. Herman, O. Torres, B. N. Holben, D. Tanre, T. F. Eck, A. Smirnov, B. Chatenet, and F. Lavenu, Comparisons of the TOMS aerosol index with Sun-photometer aerosol optical thickness: Results and applications, *J. Geophys. Res.*, 104, 6269–6279, 1999b.

Hurst, D. F., D. W. T. Griffith, J. N. Carras, D. J. Williams, and P. J. Fraser, Measurements of trace gases emitted by Australian savanna fires during the 1990 dry season, *J. Atmos. Chem.*, 18, 33–56, 1994a.

Hurst, D. F., D. W. T. Griffith, and G. D. Cook, Trace gas emissions from biomass burning in tropical Australian savannas, *J. Geophys. Res.*, *99*, 16,441–16,456, 1994b.

Johnston, T., Canada Report 2000, Canadian Interagency Forest Fire Center, 2001.

Justice, C. O., J. D. Kendall, P. R. Dowty, and R. J. Scholes, Satellite remote sensing of fires during the SAFARI campaign using NOAA advanced very high-resolution radiometer data, *J. Geophys. Res.*, *101*, 23,851–23,863, 1996.

Kasischke, E. S., and L. M. Bruhwiler, Emmisions of carbon dioxide, carbon monoxide and methane from boreal forest fires in 1998, *J. Geophys. Res.*, *107*, 8146, doi:10.1029/2001JD000461, 2002.

Kasischke, E. S., K. Bergen, R. Fennimore, F. Sotelo, G. Stephens, A. Janetos, and H. H. Shugart, Satellite imagery gives clear picture of Russia's boreal forest fires, *Eos*, *80*(144), 147, 1999.

Kaufman, Y. J., A. Setzer, D. Ward, D. Tanre, B. N. Holben, P. Menzel, M. C. Pereira, and R. Rasmussen, *J. Geophys. Res*, *97*, 14,581–14,599, 1992.

Kengen, S., and L. R. Graca, Forest policies in Brazil, in *World Forests, Society and Environment, World Forests*, vol. 1, edited by M. Palo and J. Uusivuori, Kluwer Acad., Norwell, Mass., 1999.

Kita, K., M. Fujiwara, and S. Kawakami, Total ozone increase associated with forest fires over the Indonesian region and its relation to the El Niño–Southern oscillation, *Atmos. Environ.*, *34*, 2681–2690, 2000.

Lacaux, J.-P., R. Delmas, J. C. Menaut, L. Abbadie, B. Bonsang, H. Cachier, J. Baudet, M. O. Andreae, and G. Helas, Biomass burning in the tropical savannas of Ivory Coast: An overview of the field experiment Fire of Savannas (FOS/DECAFE '91), *J. Atmos. Chem.*, *22*, 195–216, 1995.

Laursen, K. K., P. V. Hobbs, L. F. Radke, and R. A. Rasmussen, Some trace gas emissions from North America biomass fires with an assessment of regional and global fluxes from biomass burning, *J. Geophys. Res.*, *97*, 20,687–20,701, 1992.

Levine, J., The 1997 fires in Kalimantan and Sumatra, Indonesia: Gaseous and particulate emissions, *Geophys. Res. Lett.*, *26*, 815–818, 1999.

Liu, H., W. L. Chang, S. J. Oltmans, L. Y. Chan, and J. M. Harris, On springtime high ozone events in the lower troposphere from Southeast Asian biomass burning, *Atmos. Environ.*, *33*, 2403–2410, 1999.

Lobert, J., W. Keen, J. Logan, and R. Yevich, Global chlorine emissions from biomass burning: Reactive chlorine emissions inventory, *J. Geophys. Res.*, *104*, 8373–8389, 1999.

Logan, J., M. Prather, S. Wofsy, and M. McElroy, Tropospheric chemistry: A global perspective, *J. Geophys. Res.*, *86*, 7210–7254, 1981.

Malingreau, J.-P., The 1982–1983 drought in Indonesia: Assessment and monitoring, in *The Societal Impacts Associated with the 1982–1983 Worldwide Climate Anomalies*, edited by M. Glantz, R. Katz, and M. Krenz, pp. 11–18, Natl. Cent. for Atmos. Res., 1987.

Malingreau, J.-P., The contribution of remote sensing to the global monitoring of fires in tropical and subtropical ecosystems, in *Fires in the Tropical Biota, Ecosystem Processes and Global Challenges*, edited by J. G. Goldammer, pp. 337–370, Springer-Verlag, New York, 1990.

Marenco, A., J.-C. Médale, and S. Prieur, Study of tropospheric ozone in the tropical belt (Africa, America) from STRATOZ and TROPOZ campaigns, *Atmos. Environ.*, *24A*, 2823–2834, 1990.

Martin, R. V., et al., An improved retrieval of tropospheric nitrogen dioxide from GOME, *J. Geophys. Res.*, *107*, 4437, doi:10.1029/2001JD001027, 2002a.

Martin, R. V., et al., Interpretation of TOMS observations of tropical tropospheric ozone with a global model and in situ observations, *J. Geophys. Res.*, *107*(D18), 4351, doi:10.1029/2001JD001480, 2002b.

Matsueda, H., H. Y. Inoue, M. Ishii, and Y. Tsutsumi, Large injection of carbon monoxide into the upper troposphere due to intense biomass burning in 1997, *J. Geophys. Res.*, *104*, 26,867–26,879, 1999.

Menaut, J.-C., L. Abbadie, F. Lavenu, P. Loudjani, and A. Podaire, Biomass burning in West African savannas, in *Global Biomass Burning, Atmospheric, Climatic, and Biospheric Implications*, edited by J. S. Levine, pp. 133–142, MIT Press, Cambridge, Mass., 1991.

McCormick, M. P., and R. E. Veiga, SAGE II measurements of early Pinatubo aerosols, *Geophys. Res. Lett.*, *19*, 215–218, 1992.

McPeters, R. D., et al., Nimbus 7 total ozone mapping spectrometer (TOMS) data products users guide, *NASA Ref. Publ. 1384*, 1996.

Mori, T., Effects of droughts and forest fires on dipterocarp forest in East Kalimantan, in *Ecological Studies 140, Rainforest Ecosystems of East Kalimantan: El Niño, Drought, Fire and Human Impacts*, edited by E. Guhardja et al., pp. 29–45, Springer, New York, 2000.

Muraleedharan, T. R., M. Radojevic, A. Waugh, and A. Caruana, Emissions from the combustion of peat: An experimental study, *Atmos. Environ.*, *34*, 3033–3035, 2000.

Nakajima, T., A. Kigurashi, N. Takeuchi, and J. Herman, Satellite and ground-based study of optical properties of 1997 Indonesian forest fire aerosols, *Geophys. Res. Lett.*, *26*, 2421–2424, 1999.

Olson, J. R., B. A. Baum, D. R. Cahoon, and J. H. Crawford, Frequency and distribution of forest, savanna, and crop fires over tropical regions during PEM-Tropics A, *J. Geophys. Res.*, *104*, 5865–5876, 1999.

Peppler, R. A., et al., ARM southern Great Plains site observations of the smoke pall associated with 1998 Central American fires, *Bull. Am. Meteorol. Soc.*, *81*, 2563–2591, 2000.

Prospero, J. M., and T. N. Carson, Vertical and aerial distribution of Saharan dust over the Western Equatorial North Atlantic Ocean, *J. Geophys. Res.*, *77*, 2555–2565, 1972.

Radke, L. F., D. A. Hegg, P. V. Hobbs, J. D. Nance, J. H. Lyons, K. K. Laursen, R. E. Weiss, P. J. Riggan, and D. E. Ward, Particulate and trace gas emissions from large biomass fires in North America, in *Global Biomass Burning: Atmospheric, Climatic, and Biospheric Implications*, edited by J. S. Levine, pp. 394–402, MIT Press, Cambridge, Mass., 1991.

Rapalee, G., S. E. Trumbore, E .A. Davidson, J. W. Harden, and H. Velhuis, Soil carbon stocks and their rates of accumulation and loss in a boreal forest landscape, *Global Biogeochem. Cycles*, *12*, 687–701, 1998.

Rasch, P. J., W. D. Collins, and B. E. Eaton, Understanding the Indian Ocean Experiment (INDOEX) aerosol distributions with an aerosol assimilation, *J. Geophys. Res.*, *106*, 7337–7355, 2001.

Richardson, J. L., An investigation of large-scale tropical biomass burning and the impact of its emissions on atmospheric composition, Ph.D. thesis, 168 pp., Georgia Inst. of Technol., Atlanta, 1994.

Rogers, C. M., and K. P. Bowman, Transport of smoke from the Central American fires of 1998, *J. Geophys. Res.*, *106*, 28,357–28,368, 2001.

Ropelewski, C. F., and M. S. Halpert, Global and regional scale precipitation associated with El Niño/Southern Oscillation, *Mon. Weather Rev.*, *115*, 1606–1626, 1987.

Sawyer, D., The future of deforestation in Amazonia: A socioeconomic and political analysis, in *Alternatives to Deforestation: Steps Toward Sustainable Use of the Amazon Rain Forest*, edited by A. B. Anderson, pp. 265–274, Columbia Univ. Press, New York, 1990.

Seiler, W., and P. J. Crutzen, Estimates of gross and net fluxes of carbon between the biosphere and the atmosphere from biomass burning, *Clim. Change*, *2*, 207–247, 1980.

Sholes, R. J., D. E. Ward, and C. O. Justice, Emissions of trace gases and aerosol particles due to vegetation burning in southern hemisphere Africa, *J. Geophys. Res.*, *101*, 23,677–23,682, 1996.

Skinner, W. R., B. J. Stocks, D. L. Martell, B. Bonsal, and A. Shabbar, The relationship between area burned by wildland fire in Canada and circulation anomalies in the mid-troposphere, in *Biomass Burning and Its Inter-Relationships With the Climate System*, edited by J. L. Innes, M. Beniston, and M. M. Verstraete, pp. 101–125, Kluwer Acad., Norwell, Mass., 2000.

Staudt, A. C., D. J. Jacob, J. A. Logan, D. Bachiochi, T. N. Krishnamurti, and G. W. Sachse, Continental sources, transoceanic transport, and inter-hemispheric exchange of carbon monoxide over the Pacific, *J. Geophys. Res.*, *106*, 32,571–32,590, 2001.

Stocks, B. J., The extent and impact of forest fires in northern circumpolar countries, in *Global Biomass Burning: Atmospheric, Climatic, and Biospheric Implications*, edited by J. S. Levine, pp. 197–202, MIT Press, Cambridge, Mass., 1991.

Stocks, B. J., B. W. van Wilgen, W. S. W. Trollope, D. J. McRae, J. A. Mason, F. Weirich, and A. L. F. Potgieter, Fuels and fire behavior dynamics on large-scale savanna fires in Kruger National Park, South Africa, *J. Geophys. Res.*, *101*, 23,541–23,550, 1996.

Stricker, N. C. M., A. Hahne, D. L. Smith, J. Delderfield, M. B. Oliver, and T. Edwards, 1995: ATSR-2, the evolution in its design from ERS-1 to ERS-2, *ESA Bull.*, *83*, August 1995.

Sussot, R. A., D. E. Ward, R. E. Babbitt, D. J. Latham, L. G. Weger, and P. M. Boyd, *Fire Dynamics and Chemistry of Large Fires (Final Report)*, 29 pp., USDA For. Serv., Missoula, Mont., 1990.

Thomason, L. W., L. R. Poole, and T. Deshler, A global climatology of stratospheric aerosol surface area density deduced from Stratospheric Aerosol and Gas Experiment II measurements: 1984–1994, *J. Geophys. Res.*, *102*, 8967–8976, 1997.

Torres, O., P. K. Bhartia, J. R. Herman, Z. Ahmad, and J. Gleason, Derivation of aerosol properties from satellite measurements of backscattered ultraviolet radiation: Theoretical basis, *J. Geophys. Res.*, *103*, 17,099–17,110, 1998.

U.S. Department of Agriculture, *Major World Crop Areas and Climatic Profiles, World Agric. Outlook Board, Agric. Handb., No. 664*, U.S. Dep. of Agric., Washington D. C., September 1994.

Ward, D. E., and C. C. Hardy, Smoke emissions from wildland fires, *Environ. Int.*, *17*, 117–134, 1991.

Ward, D. E., R. A. Setzer, Y. J. Kaufman, and R. A. Rasmussen, Characteristics of smoke emissions from biomass fires of the Amazon region—BASE-A experiment, in *Global Biomass Burning: Atmospheric, Climatic, and Biospheric Implications*, edited by J. S. Levine, pp. 394–402, MIT Press, Cambridge, Mass., 1991.

Ward, D. E., R. A. Susott, Y. J. Kaufman, R. E. Babbitt, D. L. Cummings, B. Dias, B. N. Holben, Y. J. Kaufman, R. A. Rasmussen, and A. W. Setzer, Smoke and fire characteristics for cerrado and deforestation burns in Brazil: BASE-B experiment, *J. Geophys. Res.*, *97*, 14,601–14,619, 1992.

Weber, M. G., and B. J. Stocks, Forest fires and sustainability in the boreal forests of Canada, *Ambio*, *27*, 545–550, 1998.

Wolter, K., and M. S. Timlin, Measuring the strength of ENSO—How does 1997/98 rank?, *Weather*, *53*, 315–324, 1998.

Yevich, R., and J. A. Logan, An assessment of biofuel use and burning of agricultural waste in the developing world, *Global Biogeochem. Cycles*, in press, 2002.

———————————

B. N. Duncan, Laboratoire de Modélisation de la Chimie Atmosphérique, École Polytechnique Fédérale de Lausanne, Lausanne, Switzerland. (bryan.duncan@epfl.ch)

J. A. Logan and R. Yevich, Department of Earth and Planetary Sciences and Division of Engineering and Applied Sciences, Harvard University, Cambridge, MA, USA.

R. V. Martin, Harvard-Smithsonian Center for Astrophysics, 60 Garden Street, Cambridge, MA 02138, USA.

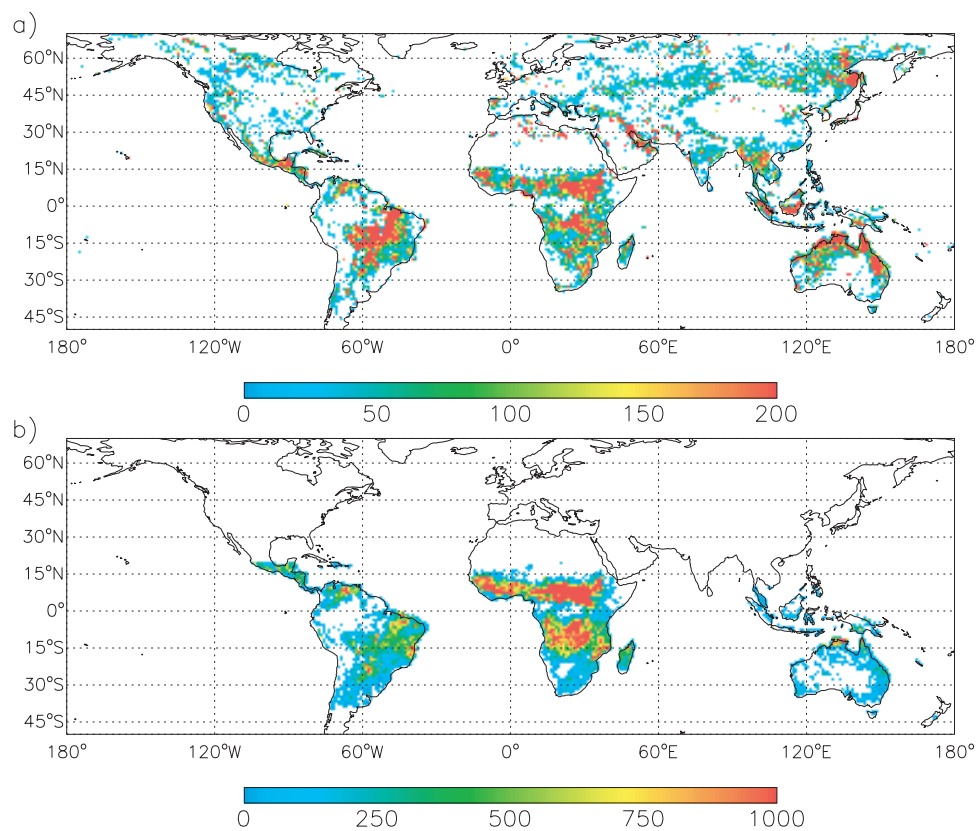A. C. Staudt, National Research Council, 500 5th Street, NW, Washington, D. C., USA.

Figure 1. Fire-counts binned into 1° × 1° grid boxes using the a) ATSR World Fire Atlas (August 1996 to December 2000) and b) AVHRR World Fire Atlas for Australia (1993), South America (1993), and Africa (July 1992 to June 1994). There was no AVHRR data available outside these three regions.
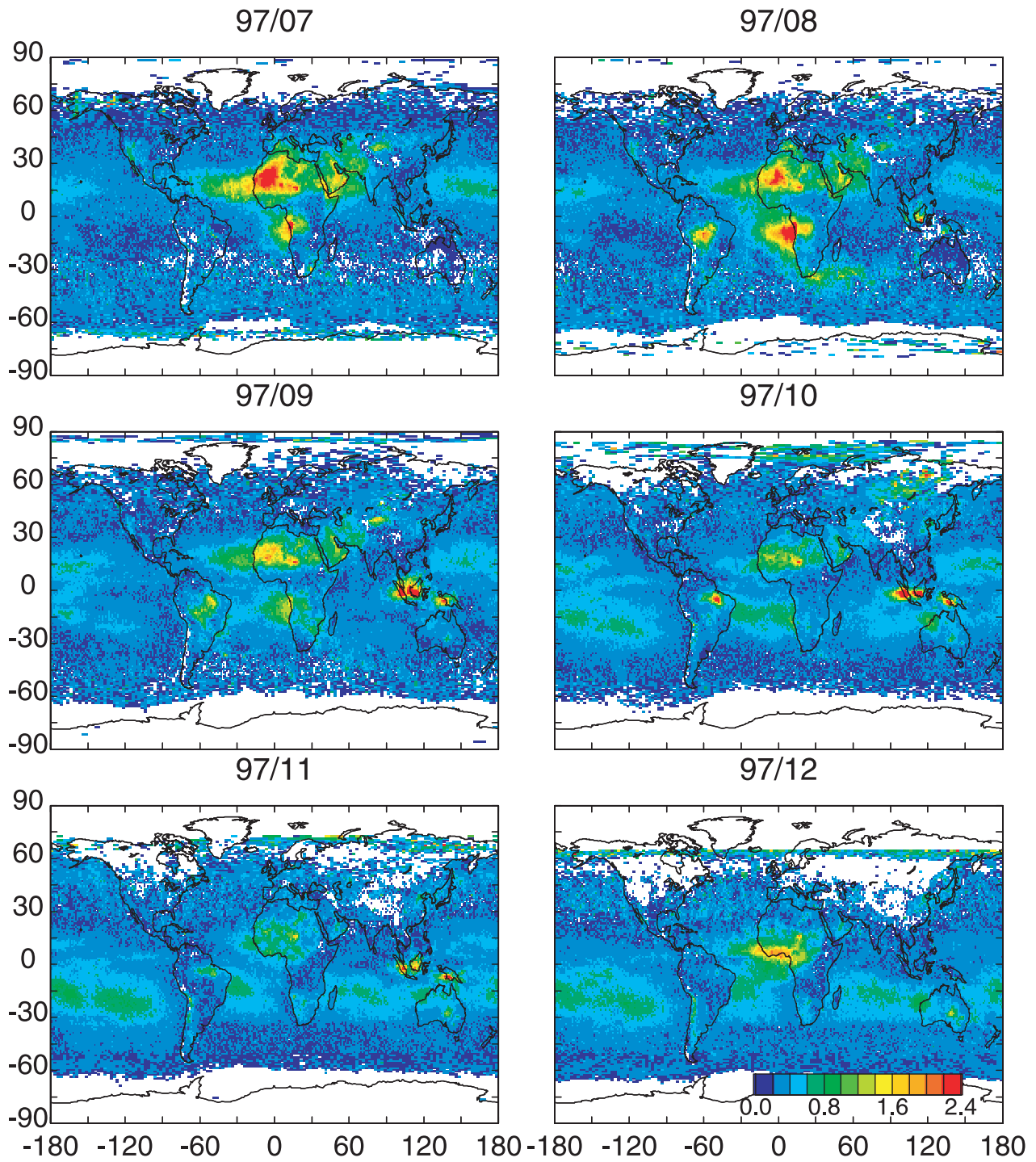
Figure 2. Monthly averaged AI as measured by TOMS for a complete year (i.e., July 1997 to June 1998).
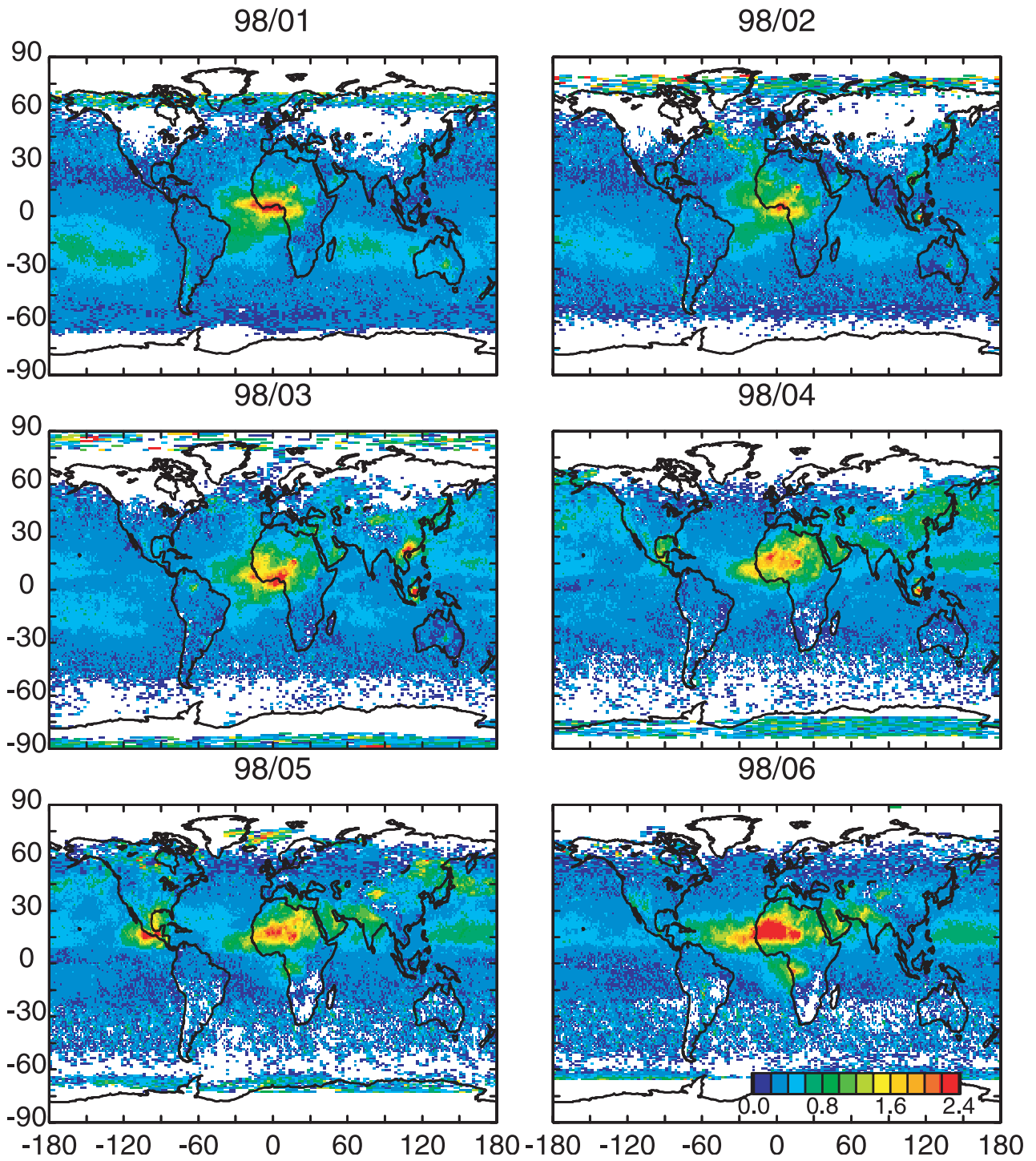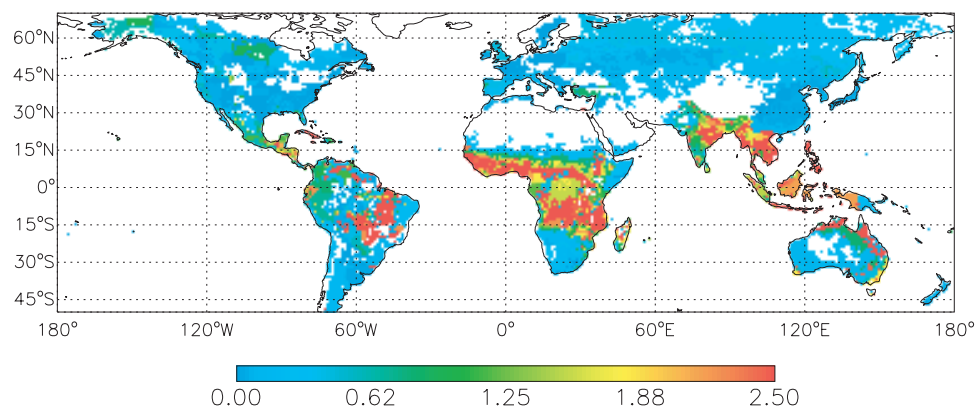
Figure 2. (continued)

Figure 4. Spatial distribution of mean CO emissions from biomass burning ($\times$ 10^{19} molecules CO cm^{-2} yr^{-1}). There are data points higher than 2.5×10^{19} molecules CO cm^{-2} yr^{-1}, however, for clarity, the scale is capped.
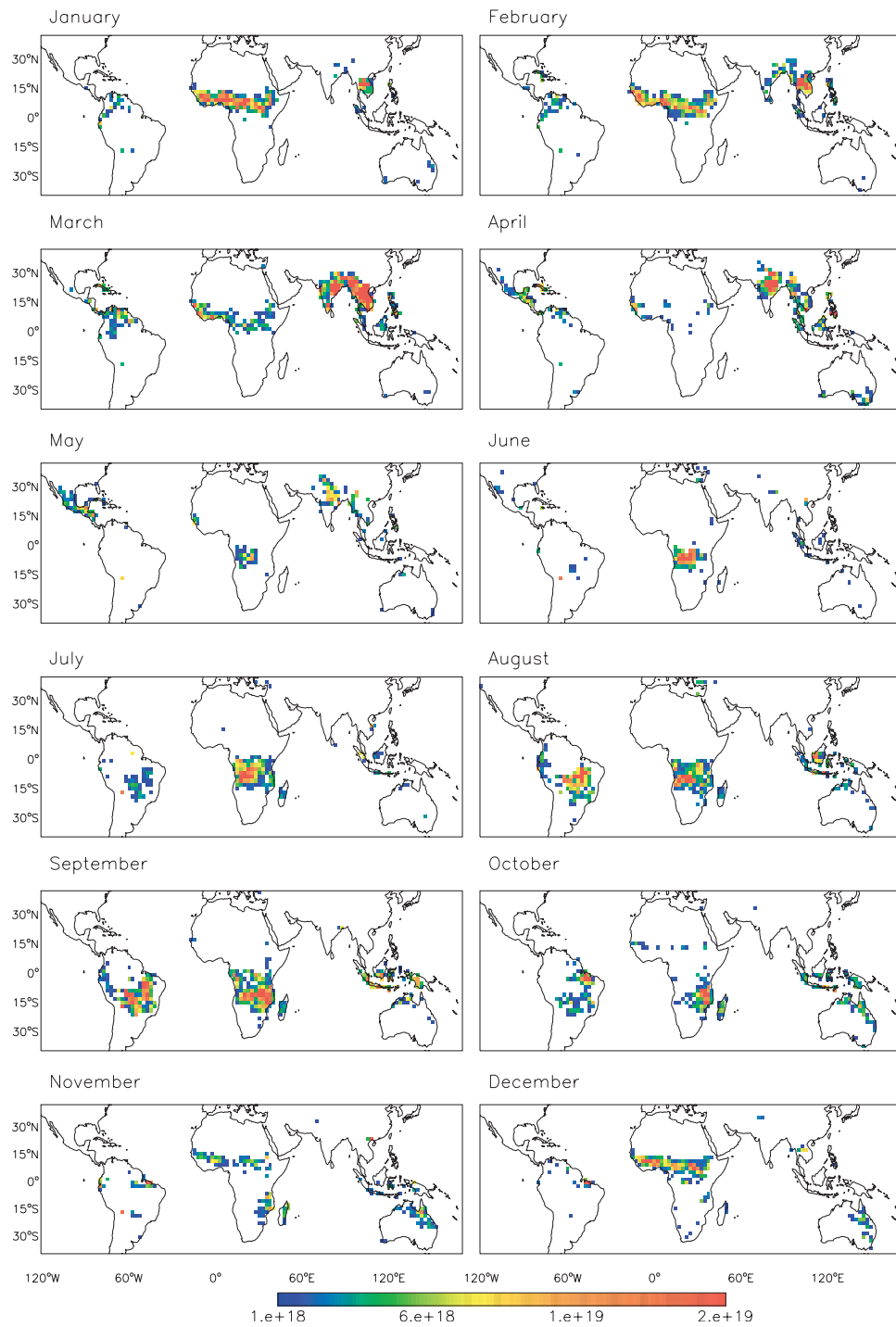
Figure 6. Mean seasonal variation in biomass burning emissions (molecules CO cm^{-2} month^{-1}).
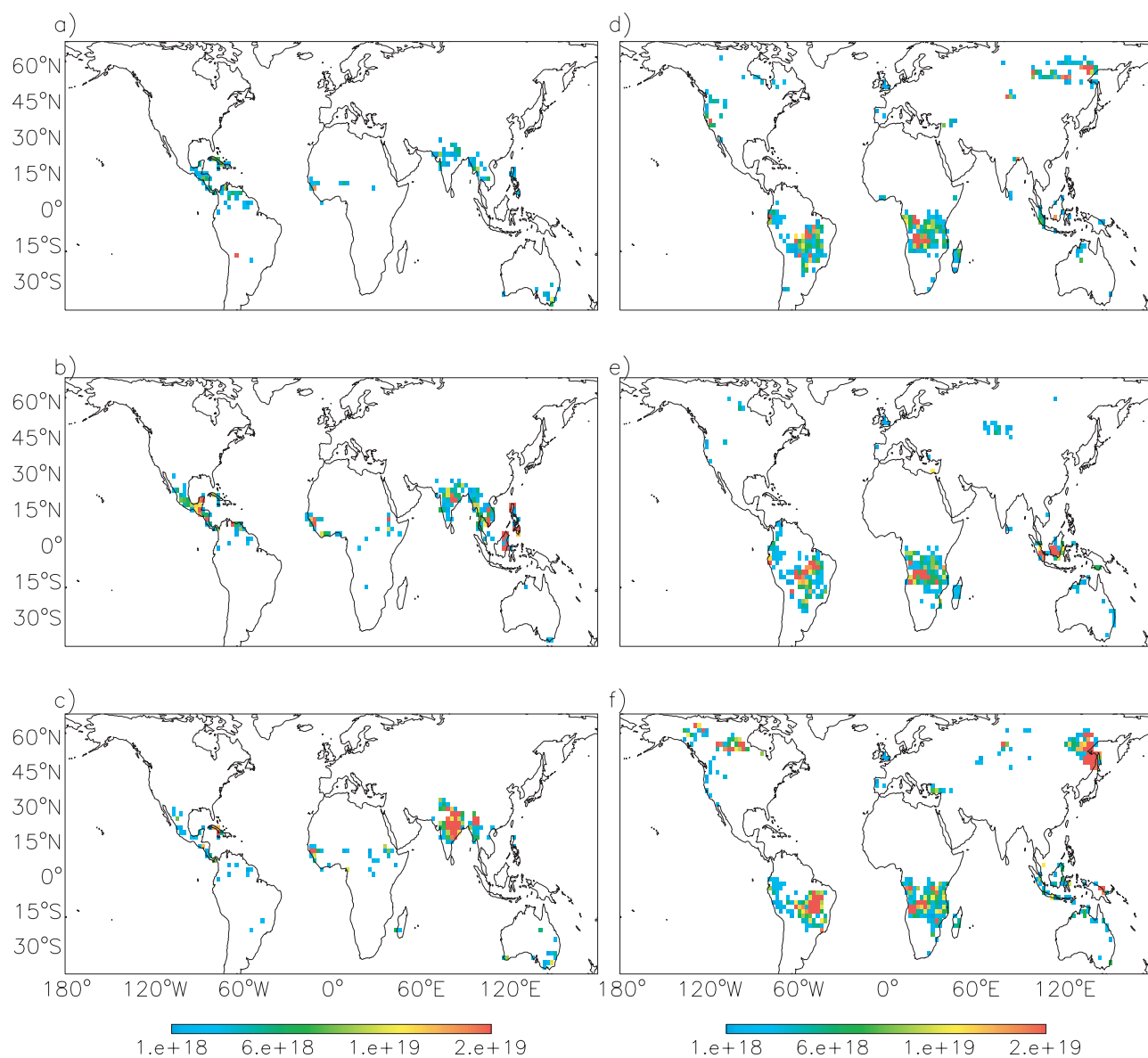
Figure 9. Interannual variation in biomass burning emissions (molecules CO cm^{-2} month^{-1}) for April a) 1997, b) 1998, and c) 1999, and August d) 1996, e) 1997, and f) 1998.